Available online at www.sciencedirect.com

ScienceDirect

Geochimica et Cosmochimica Acta 242 (2018) 165–190

Geochimica et Cosmochimica Acta

www.elsevier.com/locate/gca

Rates of dehydration of olivines from San Carlos and Kilauea Iki

Elizabeth Ferriss [a], Terry Plank [a,*], Megan Newcombe [a], David Walker [a], Erik Hauri [b]

[a] *Lamont-Doherty Earth Observatory of Columbia University, Geochemistry Division, 219 Comer Building, 61 Route 9W, Palisades, NY 10964, USA*

[b] *Department of Terrestrial Magnetism, Carnegie Institution of Washington, 5241 Broad Branch Road, NW, Washington, DC 20015-1305, USA*

Received 3 January 2018; accepted in revised form 31 August 2018; available online 11 September 2018

Abstract

The rate at which H^+ moves into, through, and out of olivine is of great interest for understanding the deep water cycle, assessing the fidelity of olivine-hosted melt inclusions as recorders of pre-eruptive melt compositions, and estimating the decompression rate of magma during volcanic eruptions. Here we conduct a series of experiments and observations on natural Fe-bearing olivine to better understand and quantify this H^+ mobility, with a particular focus on the rate at which H^+ diffuses out of olivine. We have carried out sequential dehydration experiments on single crystals of natural, Fe-bearing olivine polished and oriented along three crystallographic orientations. These efforts include four separate parts: (1) the partial hydration of polished blocks of xenolithic San Carlos olivine at 800 °C and 1000 °C, 1 GPa, and oxygen fugacity (fO_2) at the Ni-NiO buffer (NNO); (2) sequential dehydration of a homogeneous block of San Carlos olivine at 800 °C, 1-atm, and fO_2 of NNO-2.6; (3) sequential dehydration of a polished block of an olivine phenocryst from Kilauea Iki at 800 and 1000 °C, 1 atm, and fO_2 held at NNO-2.6 until the final step, which was conducted at NNO + 1.9; and (4) the measurement by secondary ion mass spectrometry of hydrogen zonation profiles in an olivine phenocryst from Kilauea Iki coupled with Monte Carlo modeling to determine total H diffusivities in a natural setting. Hydrogen zonation profiles were measured in all three crystallographic directions *a*, *b*, and *c* through the uncut blocks before and after each time step for all experiments by Fourier transform infrared spectroscopy using light polarized ‖ *a* and modeled in 3 dimensions to determine both total and peak-specific dehydration, producing over 50 sets of 3 apparent diffusivities.

The results show that the apparent diffusivity of total H^+ varies both over time and for olivines with different defect populations, and thus H^+ does not diffuse at inherently site-specific rates. These variations are due to rapid reactions that may occur between sites as a function of changing defect concentrations. Our experiments reveal three new phenomena: (1) H^+ that is associated with the Ti-clinohumite defect, [Ti-2H], can enter and exit olivine at the fastest rate measured. (2) The rate of H^+ loss from specific infrared absorption peaks, and in total, may change with progressive dehydration due to the buildup of Fe^{3+} and redistribution of defects, particularly the rehydration of [Ti-2H]. (3) The following Arrhenius laws appear to apply to total H^+ diffusion out of most natural olivines that have been studied experimentally and naturally during dehydration: $D_a = 10^{-5.4}\exp(-130/RT)$; $D_b = 10^{-6.9}\exp(-130/RT)$; and $D_c = 10^{-6.6}\exp(-130/RT)$, where R is the gas constant 8.314 J/mol K; T is the temperature, the units of the diffusivities (D) are in m^2/s; and the activation energy is 130 kJ/mol. This rate is slower than proton-polaron redox rate but faster than proton-metal vacancy diffusion and appears to characterize olivine of Fo ~90 composition in a wide range of conditions, from self-diffusion, to melt inclusion re-equilibration, to mantle xenolith and volcanic phenocryst zonation during ascent.

Keywords: Olivine; Hydrogen; Diffusion; FTIR

* Corresponding author.
E-mail addresses: ferriss@ldeo.columbia (E. Ferriss), tplank@ldeo.columbia.edu (T. Plank).

https://doi.org/10.1016/j.gca.2018.08.050
0016-7037/

1. INTRODUCTION

The diffusivity of hydrogen in olivine is a fundamental physical parameter critical for understanding a wide range of Earth and planetary processes. Hydrogen can affect global-scale phenomenon such as melting relations and rock strength, and so in turn may control mantle rheology and the occurrence of plate tectonics (Bell and Rossman, 1992; Regenauer-Lieb, 2006). Accurate knowledge of the diffusivity of hydrogen also has great potential to serve as a chronometer to determine magma ascent times from hydrogen diffusion profiles in olivine phenocrysts (Demouchy et al., 2006). Because of its close relationship to water and the bonds that H^+ forms with oxygen within the olivine structure, hydrogen incorporated in olivine and other nominally anhydrous minerals is sometimes referred to as "water" or "hydroxyl". Here we will primarily refer to this species as H^+.

H^+ may be incorporated into the olivine lattice in a variety of ways that can be distinguished by differences in the wavenumber of the O—H bonds as measured by Fourier transform infrared spectroscopy (FTIR) (Beran and Zemman, 1969; Beran and Putnis, 1983; Libowitzky and Beran, 1995; Berry et al., 2005, 2007a, 2007b; Ingrin et al., 2013). A list of the defects considered in this paper are provided in Table 1. These defects may be represented in more detail using Kröger-Vink notation (Kröger and Vink, 1956), in which V is a vacancy, a superscript indicates a positive charge relative to an ideal crystal, ‘ indicates a negative charge relative to an ideal crystal, and ^{x} no charge difference from an ideal crystal. Subscripts indicate different sites: M for octahedral metal sites normally occupied by Mg, Si for tetrahedral sites ordinarily occupied by silicon, and O for a site normally occupied by oxygen. Atoms that are not involved in any reactions are typically ignored, and we follow Kohlstedt and Mackwell (1998) by writing the incorporated H^+ as a hydroxyl, OH, on an O site. For convenience, we also provide the full chemical formula for these defects in olivine, although in reality these defects are present at only ppm levels.

Broadly, H^+ defects fall into two categories: relatively high wavenumber peaks associated with silicon vacancies (the Group I bands in Bai and Kohlstedt, 1993) and relatively low wavenumber peaks associated with magnesium vacancies (the Group II bands in Bai and Kohlstedt, 1993). The Ti-clinohumite defect that involves a Ti^{4+} on a metal site, $2H^+$, and a Si vacancy, labeled here [Ti-2H], has been suggested to control mantle rheology (Faul et al., 2016) and manifests as a doublet of peaks at 3525 and 3573 cm^{-1} (Berry et al., 2007a, 2007b). Multiple other high wavenumber peaks (3450–3620 cm^{-1}) represent $4H^+$ ions charge-balanced by a Si^{4+} vacancy and are labeled here [Si-4H]. Some lower wavenumber peaks (3300–3400 cm^{-1}) appear when a Mg^{2+} vacancy is charge-balanced by a H^+ and a trivalent cation on a Mg^{2+} site. These defects are labeled as [Fe^{3+}-H], because we assume in our discussion that Fe^{3+} is the trivalent cation, although Al^{3+} and/or Cr^{3+} may also be important H^+ storage sites in some olivines (Berry et al., 2005). Low wavenumber peaks between 3200 and 3250 cm^{-1} have been associated with $2H^+$ charge-balancing a Mg^{2+} vacancy, and these defects are labeled here [Mg-2H]. The different mechanisms are important because the rate at which H^+ moves through the lattice may vary for each defect (Padrón-Navarta et al., 2014).

Previous work on the diffusivity of H^+ in olivine has produced a 6-order-of-magnitude range of measurements, from $10^{-9.7}$ m^2/s during the first hour of hydrating San Carlos olivine at 1000 °C (Mackwell and Kohlstedt, 1990) to $10^{-15.7}$ m^2/s for the decrease in hydrated Si vacancies, [Si-4H], from synthetic forsterite during dehydration at the same temperature (Padrón-Navarta et al., 2014). The calculated activation energies suggest even larger discrepancies at lower temperatures. This range has led to considerable disagreement about the correct diffusivity and approach to apply to a given application. The observation of differences in H^+ loss profiles for different FTIR peaks (e.g., Tollan et al., 2015) is particularly important. Because FTIR peaks must then be resolved and analyzed individually, H^+ data from secondary ion mass spectrometry (SIMS), a powerful technique, becomes significantly more difficult to interpret because SIMS measures only the total H^+, the sum of the profiles for various H species.

Total H^+ diffusion in natural olivine has been observed to occur at two different rates during hydration under pressure (Kohlstedt and Mackwell, 1998; Demouchy and Mackwell, 2006). The faster of these two rates was attributed to a flux of H^+ charge-balanced by a flux of electrons from Fe^{2+} to Fe^{3+}. Because they distort the local lattice, the electron holes associated with Fe^{3+} are often called polarons, and so this "redox" rate has also sometimes been labeled proton-polaron or PP. The slower rate was attributed to a migration of metal vacancies parallel to the main flux direction of the H^+ gradient and so was referred to as the proton-vacancy (PV) rate. Neither of these studies note any significant differences between IR peaks, and

Table 1
List of hydrous and anhydrous defects in olivine considered in this paper. Descriptions of the notation are provided in the introduction.

Defect label	Kröger-Vink notation	Olivine formula	FTIR peak location (cm^{-1})
[Ti-2H]	$Ti_{Si}^{\bullet\bullet} - V_{Si}'''' - 2OH_O^{\bullet}$	$MgTiH_2O_4$	3525, 3573
[Ti-2Fe^{3+}]	$Ti_{Si}^{\bullet\bullet} - V_{Si}'''' - 2Fe_M^{\bullet}$	$MgTiFe_2SiO_8$	None
[Si-4H]	$V_{Si}'''' - 4OH_O^{\bullet}$	$Mg_2H_4O_4$	3600
[Si-2H]	$2Fe_M^{\bullet} - V_{Si}'''' - 2OH_O^{\bullet}$	$Fe_2H_2O_4$	3600
[Si-4Fe^{3+}]	$V_{Si}'''' - 4Fe_M^{\bullet}$	Fe_4SiO_8	None
[Fe^{3+}-H]	$Fe_M^{\bullet} - V_M'' - OH_O^{\bullet}$	$FeHSiO_4$	3356
[M-2Fe^{3+}]	$2Fe_M^{\bullet} - V_M''$	$MgFe_2Si_2O_8$	None

subsequent work has generally assumed that dehydration proceeds similarly for total H^+, first at the redox rate and then at the PV rate (Demouchy and Bolfan-Casanova, 2016; Thoraval and Demouchy, 2014).

Significant disagreement exists about which set of diffusivities to apply in a given situation. For example, some studies of olivine phenocrysts conclude that the redox rate applies (Hauri, 2002; Le Voyer et al., 2014), whereas others suggest using the PV rate (Portnyagin et al., 2008; Chen et al., 2011; Gaetani et al., 2012). Xenolith studies face similar uncertainty, with some studies mostly focusing on choosing between redox and PV rates (Demouchy et al., 2006; Peslier and Luhr, 2006; Denis et al., 2013; Thoraval and Demouchy, 2014) and others exploring peak-specific behavior and diffusivities (Hilchie et al., 2014; Tollan et al., 2015; Peslier et al., 2015).

The major goal of this work is to better understand which diffusivity to use for applications that involve H^+ diffusion in natural olivine. We focus our efforts mostly on dehydration, for which few experimental studies exist on natural Fe-bearing olivine despite the importance of this parameter for determining the ascent rate for xenoliths and phenocrysts.

2. METHODS

We provide, for the first time, time-series data showing H^+ loss from the same single crystal of Fe-bearing olivine. We carry out such a time series for two natural olivines: a partially hydrated xenolithic olivine from San Carlos and a phenocryst from Kilauea Iki. These data are coupled with independent estimates of the H^+ diffusivity based on H^+ zonation patterns in a second Kilauea Iki phenocryst to produce a set of generic Arrhenius laws for H^+ diffusion in natural olivine with forsterite numbers between 86 and 90.

2.1. Sample selection

Olivines from San Carlos, AZ and Kilauea Iki were chemically characterized and used for H^+ diffusion experiments. The San Carlos olivine was provided by David Kohlstedt and is similar to that used in previous hydration experiments. Here we extend that work by examining site-specific dehydration behavior. The Kilauea Iki olivines were provided by David Ferguson and were collected from scoria from the 1959 Episode 1 eruption of Kilauea Iki (layer ρ17 of Stovall et al., 2011). Ferguson et al. (2016) estimated a temperature of 1192 °C and a decompression rate of 0.05 MPa/s for this eruption and suggest that these olivines quenched at 1 bar. The Kilauea Iki samples are of great interest because they provide the first direct experimental measurements of H^+ diffusion in all 3 crystallographic directions of inclusion-free olivine phenocrysts relevant to volcanic systems at low pressure. We also determine for the first time hydrogen zonation profiles in natural, untreated olivine phenocrysts (from the same Kilauea Iki sample).

2.2. Sample preparation

A large crack- and inclusion-free piece of San Carlos olivine, SC1 (IGSN: IEFERSCO1), was oriented by Laue camera at Cornell University and then cut into a series of smaller pieces approximately 2–3 mm long on each side using a diamond saw. One of the resulting sub-pieces, SC1-1 (IGSN: IEFERJAI3), was polished with 0.25 μm diamond paste and used to estimate the initial H^+ concentration by FTIR. Additional pieces of SC1 were used to test the hydration procedure, and pieces SC1-7 (IGSN: IEFERJAI9) and SC1-2 (IGSN: IEFERJAI4) were partially hydrated and then polished with 0.25 μm diamond paste for FTIR. SC1-2 was then sequentially dehydrated with FTIR profiles measured after each dehydration step and afterwards analyzed by electron microprobe analysis (EMPA), SIMS, and laser-ablation inductively coupled mass spectrometry (LA-ICP-MS). Table 2 outlines the experimental treatment of each crystal piece.

Two large, relatively clear pieces of the Kilauea Iki olivine were selected, oriented based on crystal morphology, and polished. The orientation of both samples was confirmed by electron backscatter diffraction (EBSD) at the American Museum on Natural History. One of these samples, Kiki (IGSN: IEFERJAIC), was polished into a block shape of dimensions 2 × 1 × 1.3 mm and characterized by EMPA, SIMS, and polarized FTIR. The sample was initially zoned in H^+, and the low H^+ rims were polished off to create a homogeneous initial block for use in dehydration experiments.

This zonation was not polished off the second Kilauea Iki phenocryst (Kikin; IGSN: IEMN1KI02), which was used to obtain an independent estimate of the total H^+ diffusivity in olivine as degassing took place during ascent. This sample was polished to its midpoint to expose the (010) plane and prepared for SIMS following recently developed sample preparation techniques for reducing instrumental background (Mosenfelder et al., 2011; Le Voyer et al., 2014; Newcombe et al., 2017a). The phenocryst was cleaned in ultrasonic baths of toluene, acetone, and isopropanol; baked under vacuum at 110 °C for ~72 h; pressed into a 1-in. round aluminum mount containing indium metal; and coated in Au. The sample and probe were degassed for three days prior to analysis.

Sample thicknesses were measured with a digital micrometer accurate to within ±5 μm. Additional details for samples, including images and sample dimensions, are available online at geosamples.org.

2.3. Characterization by EMPA and LA-ICP-MS

Major elements of SC1-2 and Kiki were analyzed by electron microprobe analysis (EMPA) at the American Museum of Natural History (AMNH) along traverses parallel to those on which H^+ measurements were made to confirm homogeneity of the samples prior to dehydration. The beam current was 20 nA, and the accelerating voltage was 15 kV.

Table 2
Experimental conditions for San Carlos olivine samples SC1-7 and SC1-2 and Kilauea Iki olivines Kiki. The conditions experienced by the natural Kilauea Iki sample Kikin (from Helz et al. (2017)) are included for comparison.

Sample name	Temperature (Celsius)	Pressure (GPa)	fO_2 Buffer	log fO_2 in bars	Heating time (hours)	Total dehydration time at constant temperature (hours)
SC1-7	1000	1	NNO	−10.3	7	–
SC1-2	800	1	NNO	−13.9	17.4	–
SC1-2	800	0.0001	NNO − 2.6	−16.5	1	1
SC1-2	800	0.0001	NNO − 2.6	−16.5	2	3
SC1-2	800	0.0001	NNO − 2.6	−16.5	4	7
SC1-2	800	0.0001	NNO − 2.6	−16.5	6	13
SC1-2	800	0.0001	NNO − 2.6	−16.5	6	19
SC1-2	800	0.0001	NNO − 2.6	−16.5	24	43
SC1-2	800	0.0001	NNO − 2.6	−16.5	25	68
Kiki	800	0.0001	NNO − 2.6	−16.5	1	1
Kiki	800	0.0001	NNO − 2.6	−16.5	7	8
Kiki	1000	0.0001	NNO − 2.6	−13.1	3	3
Kiki	1000	0.0001	NNO − 2.6	−13.1	3	6
Kiki	1000	0.0001	NNO − 2.6	−13.1	1	7
Kiki	1000	0.0001	NNO + 1.9	−8.4	1	8
Kikin	1200	0.0001	NNO − 0.3	−8.0	N/A	N/A

LA-ICP-MS traverses were conducted to measure MgO, SiO_2, P, Sc, Ti, V, Cr, MnO, FeO, Co, Ni, and Zn in samples SC1-2, SC1-7, Kiki, and Kikin, plus Li, Al, CaO, and Cu in the Kilauea Iki samples using a Thermo/VG PQ ExCell and ESI 193 nm excimer laser at the Lamont-Doherty Earth Observatory (LDEO) after all experiments were complete. The crystals were rastered from core to rim at 5 μm/s using a 50-μm spot size, 15 Hz, and 2.4 GW/cm^2 following a pre-ablation step to clean the sample surface. The 50 μm raster was chosen to provide good quality data (generally 1–3% relative standard deviation) at the single ppm level for transition metals. Background was collected for 1 min with the laser firing. The average background was subtracted from the signal, which was then averaged in 15–20 μm blocks. SC1 samples were corrected for drift assuming constant Si. Drift correction was unnecessary for Kilauea Iki samples. Mg was used as an internal standard (based on EMPA data) for all samples. Initial counts were calibrated using the BIR-1 g glass (values in Kelley et al., 2003), then corrected to the certified or proposed values for San Carlos olivine (USNM 111312/444), after Ruprecht and Plank (2013).

2.4. Initial H^+ concentrations by FTIR and NanoSIMS

The initial H^+ concentration in each olivine used in dehydration experiments was estimated using both polarized FTIR and NanoSIMS. Polarized FTIR measurements were performed at AMNH using the Thermo Nicolet Nexus 670 infrared spectrometer and Thermo Nicolet Continuum 15× infrared microscope with a resolution of 4 cm^{-1}, spot sizes of 100 × 100 μm, an average of 200 scans, and a ZnSe polarizer. Initial H^+ concentrations were estimated from 3 orthogonal polarized measurements (Libowitzky and Rossman, 1996; Shuai and Yang, 2017) by applying the Bell and Withers calibrations (Bell et al., 2003; Withers et al., 2012). To account for the large error associated with baseline choice, 3 different baselines were drawn, and the resulting areas were averaged. Traverses along all three directions did not show significant zonation in total or peak-specific H^+ in the untreated samples.

The C, H, F, P, and Cl concentrations were measured by NanoSIMS at the Department of Terrestrial Magnetism in the Carnegie Institution in Washington, DC (DTM) along traverses parallel to *c* in SC1-2 and parallel to *b* in Kiki using calibrations similar to those for the SIMS analyses below. These NanoSIMS measurements were made before Kiki was dehydrated but after the final dehydration heating step for SC1-2. The area under the O—H stretching peaks with the electric vector E ∥ *a* is equal to that of both the untreated SC1-1 (7 ± 5 cm^{-2}) and of the partially hydrated and then dehydrated SC1-2 (7 ± 6 cm^{-2}). Because the area is the same we assume that the final H concentration is roughly equal to the initial, and so the SIMS measurements of the hydrated and then dehydrated SC1-2 were taken as a reasonable estimate of the initial water concentration in SC1.

2.5. SIMS on untreated Kilauea Iki olivine

Hydrogen profiles along the *a* and *c* crystallographic axes in the naturally zoned Kilauea Iki phenocryst (Kikin) were measured by SIMS using the Cameca 6f-SIMS at DTM. Analyses were performed using a primary beam current of ~16 nA. The primary beam was rastered across a 35 × 35 μm area during 300 s of presputtering, and the area of the raster was reduced to 20 × 20 μm during analysis. Use of a circular field aperture with a ~10-μm diameter ensured that only ions from the central ~78 μm^2 of the analytical crater were collected. Counts of ^{12}C, $^{16}O^1H$, ^{19}F, ^{30}Si, ^{31}P, ^{32}S, and ^{35}Cl were detected by an electron multiplier. The following linear relationship between $^{16}O^1H/^{30}Si$ and H^+ concentration was defined by measurements of olivine and orthopyroxene: H_2O (ppm) =

$3792 \times {}^{16}O^{1}H/{}^{30}Si$ ($R^2 = 0.78$). Background counts of $^{16}O^{1'}H$ were assessed via frequent analysis of nominally dry Suprasil 3002 silica glass (purchased from Heraeus Quarzglas, Switzerland). Replicate analyses of Suprasil glass indicate that the detection limit of our water analyses was 1.5 ppm H2O following the methodology of Long and Winefordner (1983). Analytical drift throughout the session was monitored by frequent analysis of Herasil 102 silica glass (purchased from Heraeus) containing ~55 ppm H_2O.

2.6. Hydration of San Carlos olivine

Two pieces of previously oriented San Carlos olivine SC1, SC1-2 and SC1-7, were partially hydrated in a ¾" Boyd-type piston cylinder apparatus with a $BaCO_3$ pressure medium using a procedure broadly similar to that of Jollands et al. (2016). Here the samples were placed in copper capsules and surrounded by liquid distilled H_2O and a powdered mixture of Ni and NiO to control oxygen fugacity and San Carlos olivine and enstatite to control silica activity (Fig. 1). The Ni-NiO buffer was chosen for comparison with previous experimental work (e.g., Mackwell and Kohlstedt 1990; Demouchy and Mackwell, 2006), and copper was chosen because of its low reactivity and high melting point relative to gold and silver, thus allowing higher experimental temperatures. Copper also permits access to a wider range of pO_2 conditions than Ag.

Temperatures were controlled with a D-type thermocouple (W3%Re-W25%Re) with control precision of ±2 °C and probable accuracy of ±20 °C. After rapid quenching followed by relatively slow decompression, the capsules were pierced with a drill to confirm water was still present at the end of the experiment and then dissolved overnight in a mixture of 1:1 H_2O to HNO_3. The rectangular parallelepiped samples were then mounted in CrystalBond, polished with 0.25 μm diamond paste on all sides, and cleaned in acetone.

SC1-2 was hydrated at a nominal temperature of 800 °C and 1 GPa pressure, which corresponds to a water fugacity of 1.6 GPa (Withers, 2013), for 17.5 h. That time was chosen in order to reach, but not pass, what Kohlstedt and Mackwell (1998) call "metastable equilibrium". If the model used by Kohlstedt and Mackwell (1998) is correct, the H^+ concentration in SC1-2 after the piston cylinder experiment should be homogeneous, and the concentration should be lower than the true solubility and presumably determined by the initial concentration of ferric iron. The metastable equilibrium H^+ concentration was both large enough to easily measure and homogeneous, and therefore SC1-2 was a suitable starting material for step-wise dehydration experiments.

SC1-7 was heated for 7 h at 1 GPa and temperature readings of 1000 °C. After quenching and removing the Cu and sample from the piston cylinder, we observed that the Cu canister had visibly changed shape in a way that was consistent with having partially melted, and some of it had protruded into the C furnace. This partial melting suggests the true temperature in the capsule was closer to 1085 °C (the melting point of copper), or, more likely, the Cu was contaminated, perhaps with a small amount of oxygen, resulting in freezing point depression. This temperature range and pressure correspond to water fugacities of 1.9–2.0 GPa (Withers, 2013). Within this temperature range, given the dimensions of the sample and the diffusivities reported by Kohlstedt and Mackwell (1998), the experiment time of 7 h should allow the completion of redox-rate diffusion and initiation of diffusion at the slower PV rate without fully saturating the sample. This experiment allows

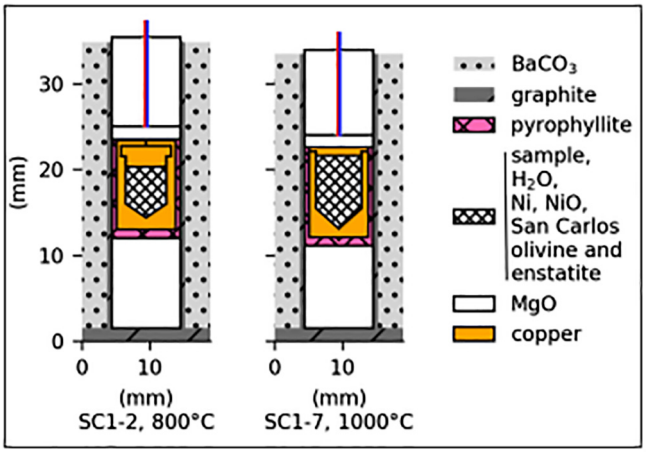

Fig. 1. Schematic cross-sections illustrating the experimental design for hydrating San Carlos olivine samples SC1-2 and SC1-7 in a piston cylinder apparatus showing the $BaCO_3$ pressure medium, graphite furnace and pyrophyllite sleeve surrounding an unwelded copper capsule containing the sample, liquid water, and a powdered mixture of nickel, nickel oxide, San Carlos olivine, and San Carlos enstatite. The sleeve and capsule are supported by MgO, and D-type W-Re thermocouples in Al_2O_3 ducts (colored lines) extend through cylindrical holes in the MgO. Minor differences in the capsule shapes are a result of differences in Cu machining techniques. (For interpretation of the references to colour in this figure legend, the reader is referred to the web version of this article.)

a direct comparison with previous work (Mackwell and Kohlstedt, 1990; Kohlstedt and Mackwell, 1998; Demouchy and Mackwell, 2006).

2.7. Dehydration

Olivine samples SC1-2 (the same sample that was partially hydrated according to the procedure described above) and Kiki (untreated) were dehydrated in increments using the vertical furnace used in previous dehydration experiments (Ferriss et al., 2015, 2016). Samples were suspended in the furnace by a wire (60% Au, 40% Pd), and the oxygen fugacity was controlled with a mixture of CO and CO_2. The partially hydrated sample SC1-2 was heated at 800 °C for 1, 3, 7, 13, 19, 43, and 68 h at an oxygen fugacity $10^{-16.5}$ bars, equivalent to NNO-2.6, where NNO is the nickel-nickel oxide buffer. Oxygen fugacity was monitored with a zirconia sensor. Kiki was heated at 800 °C for 1 and 8 h; then 3, 6, 7, and 8 h at 1000 °C. All heating steps for Kiki were conducted at oxygen fugacity of NNO-2.6 except for the final step at 1000 °C, which was conducted at relatively oxidizing conditions, NNO + 2. A summary of all experimental run conditions is provided in Table 2. The oxygen fugacity values were calculated assuming one bar total pressure using the regression of data of O'Neill (1987) from Herd (2008).

2.8. FTIR analyses of treated samples

Before heat treatment and in between each heating step, samples were analyzed by polarized FTIR along 3 orthogonal traverses parallel to the three crystallographic directions in the uncut crystal (Fig. 2). For brevity and consistency with our previous work on clinopyroxene (Ferriss et al., 2016), we use the labels *a*, *b*, and *c* to represent the 3 directions that correspond to [100], [010], and [001]. These FTIR analyses use the same conditions described above to estimate the initial water and were in all cases conducted with polarized radiation with the electric vector E ∥ *a* to provide a consistent set of measurements for each direction with high areas under the O—H stretching peaks (Fig. 3). Quadratic baselines were drawn based on the curve of the spectrum of the untreated and/or the dehydrated sample, with typical wavenumber ranges of 3200–3700 cm^{-1}. Each profile was normalized to the initial measurements to produce a ratio of the final to initial area A/A_0 and scaled up to a true concentration based on the initial concentrations, A_0, determined above. These "whole-block" concentrations represent the average concentration through the entire path of the infrared beam and could be used to determine diffusivities in all three crystallographic directions following the fitting procedure described below (after Ferriss et al., 2015).

To explore possible differences among various H^+ defects, the same normalization and fitting procedures were applied to individual peaks using the peak heights relative to the quadratic baseline. Particular emphasis was placed on peaks at the following 4 wavenumbers: 3600, 3525, 3356, and 3236 cm^{-1}. The peak at 3600 cm^{-1}, designated [Si-4H], is most likely $4H^+$ in a Si^{4+} vacancy with a nearby Fe^{2+} (Blanchard et al., 2017). The peak at 3525 cm^{-1}, designated [Ti-2H], is one of two prominent peaks produced by the Ti-clinohumite defect: $2H^+$ coupled with a Si^{4+} vacancy and a Ti^{4+} on a metal site. We focus on this peak both to minimize interference with nearby [Si-4H] peaks and to

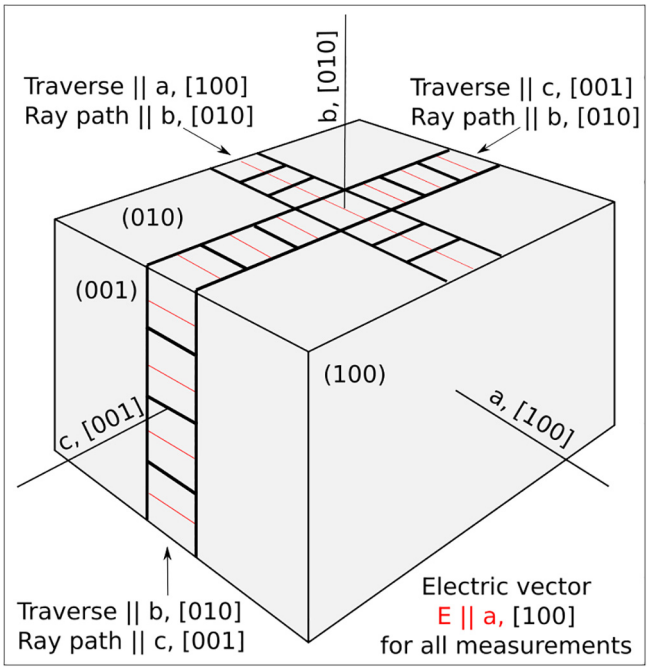

Fig. 2. Schematic illustration of the orientations of the traverses, ray paths, and electric vectors used to collect FTIR profiles for diffusion modeling, including standard indices in square brackets and labels *a*, *b*, and *c* used throughout the text and figures.

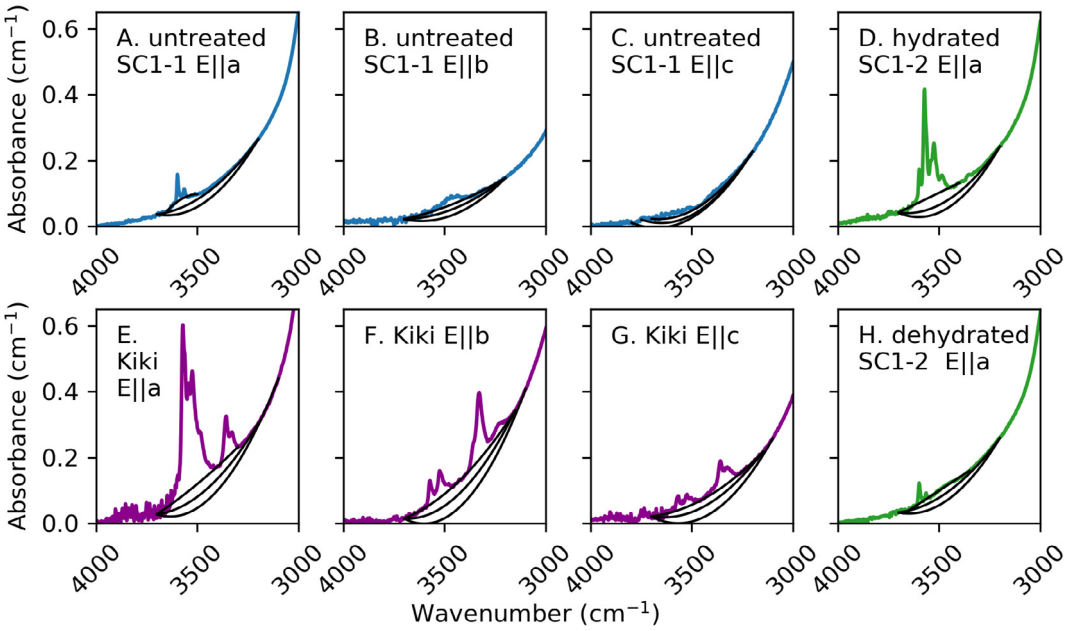

Fig. 3. Polarized FTIR spectra and baselines (black) used to estimate the H^+ concentrations of Kilauea Iki olivine (Kiki) and San Carlos olivine (SC1-1 and SC1-2) reported in Table 3. E is the electric vector of the infrared beam. Expanded views with peaks labeled are available in Figs. 4 and 6 and the Supplement.

more directly compare with the results of Padrón-Navarta et al. (2014). The 3356 cm^{-1} peak, designated [Fe^{3+}-H], is the most prominent peak in a doublet associated with a Mg^{2+} vacancy charge-balanced by H^+ and Fe^{3+} substituting on a metal site (Blanchard et al., 2017), and the 3236 cm^{-1} peak, designated [Mg-2H], is likely $2H^+$ charge-balanced by a Mg^{2+} vacancy (Berry et al., 2005).

2.9. Diffusion modeling

H^+ diffusivities in each direction were obtained from the whole-block FTIR data after each time step using forward models modified to account for path integration effects. The 3-dimensional internal concentration, v, is calculated from the time t and diffusivities D in each direction for a rectangular parallelepiped with unit initial concentration and zero external concentration for the region $0 < x < L_a$, $0 < y < L_b$; $0 < z < L_c$ as follows (Carslaw and Jaeger, 1959):

$$v = \left(\mathrm{erf}\left(\frac{x}{2\sqrt{D_a t}}\right) + \mathrm{erf}\left(\frac{L_a x}{2\sqrt{D_a t}}\right)\right) \times \left(\mathrm{erf}\left(\frac{y}{2\sqrt{D_b t}}\right) + \mathrm{erf}\left(\frac{L_b y}{2\sqrt{D_b t}}\right)\right) \times \left(\mathrm{erf}\left(\frac{z}{2\sqrt{D_c t}}\right) + \mathrm{erf}\left(\frac{L_c z}{2\sqrt{D_c t}}\right)\right) \quad (1)$$

The internal concentrations are then averaged along the ray path of the FTIR observations to obtain path-integrated profiles. These "whole-block" profiles are then fit to the data measured in the uncut block. These models are described in more detail by Ferriss et al. (2015) and were implemented using the free, open-source python software package pynams (Ferriss, 2018).

For the SIMS profiles of the zoned Kilauea Iki phenocryst, we estimated the diffusivity using a Monte Carlo model of diffusive H^+ loss from the olivine phenocryst in response to syneruptive degassing of its host magma. We assume that the volatile concentration of the host magma follows a closed-system degassing path (Witham et al., 2012). We use a 1-dimensional (1D) finite element model, which is appropriate if a central concentration plateau is observed along [100] and suggests that H^+ diffusion has not reached the center of the crystal (Thoraval and Demouchy, 2014, Shea et al., 2015). The concentration of H^+ dissolved in olivine in equilibrium with the degassing magma (i.e., the boundary condition at the exterior edge of the crystal) is calculated at each time step with a partition coefficient Kd. The diffusivity of H^+, the magma decompression rate (dP/dt), and the partition coefficient are treated as free parameters in the model, and we assume that these parameters are constant throughout the ascent history of the phenocryst. This assumption of a constant diffusivity during magma ascent at Kilauea is justified by the results of Newcombe et al. (2017b), who find that Kilauea Iki magmas ascended approximately isothermally, and by the limited pressure range experienced by the Kilauea Iki magma during ascent through the crust (1100–1 bar; Ferguson et al., 2016) and the relative insensitivity of water diffusivity to pressure (Demouchy et al., 2016). Best-fit values of these parameters were determined via least-squares fitting to 100 synthetic water concentration profiles generated by assuming each H^+ concentration measurement is normally distributed with a mean corresponding to the measured value and a standard deviation of 0.3 ppm H_2O. The least-squares minimization was performed using the 'fminsearch' MATLAB function. Starting values of D, dP/dt, and Kd were drawn at random from the

following uniform distributions spanning suitable ranges: $-9 < \log D\ (m^2/s) < -11$; $0.045 < dP/dt\ (MPa/s) < 0.055$; and $0.0011 < Kd < 0.0015$.

3. RESULTS

Detailed traverse information and standard measurements for all of the data discussed below are provided in the supplementary tables, and the original FTIR and SIMS data files along with all computer code used to analyze them are provided separately (Ferriss and Newcombe, 2018; available online at http://doi.org/10.5281/zenodo.1318324).

3.1. Characterization of the starting material

Microprobe analysis did not reveal any significant zonation in major elements along the measured profiles and were generally consistent with previous work with somewhat lower forsterite numbers: 87.7 ± 0.2 in SC1-2 and 86.2 ± 0.2 in Kiki. The San Carlos olivine used in previous H^+ diffusion experiments had a reported approximate composition with forsterite number 91 (Mackwell and Kohlstedt, 1990). This large difference in forsterite content suggests that the San Carlos olivine that we are using came from a different xenolith than the samples used in previous work.

LA-ICP-MS profiles revealed some zonation in all of the samples. The partially hydrated sample SC1-7 showed the least obvious zonation of the four samples measured, although a subtle increase is apparent in Fo (88.3–88.6 from core to rim) and Ti (36–37.5 ppm from core to rim). The Ni drops from 2600 to 2510 ppm at the rim, indicating no contamination of the olivine as a result of using Ni and NiO to buffer the oxygen fugacity over the short duration of this run (7 h at 1000 °C). The dehydrated sample SC1-2 also shows a subtle increase in Fo to the rim (88.8–89.1) driven by a small drop in FeO (10.6–10.3), while some of the transition metals show clear decreasing trends to the rim (100 ppm drop in Ni and 5–10 ppm drop in Cr, Co and Zn). These variations, particularly in elements known to relate to H^+ incorporation and movement (Fe, Cr), may explain the occasional asymmetry and lack of smoothness in the measured H^+ profiles in the San Carlos samples.

The Kilauea Iki samples showed more pronounced zonation, particularly in Kikin, for which rims were not polished off. Kikin has a lower Fo core (84.8) than Kiki (86.4 by LA-ICP-MS) and shows an increase in Fo near the rim that is consistent with previous observations that were interpreted as a recharge event months before the 1959 Kilauea Iki eruption (Rae et al., 2016). Clear zonation is also apparent in other elements that may affect H^+ incorporation and movement, notably Al (350–200 ppm) and V (9–7 ppm), which decrease toward the rims in Kikin parallel to both *a* and *c*, as well as Ti (100–120 ppm), which increases toward the rim parallel to c. This zonation in trace elements may have contributed to some of the H^+ zonation. However, the trace elements are zoned along both the *a* and *c* axes in Kikin, whereas H^+ is zoned only parallel to *a* in the same crystal, which suggests that the observed H^+ zonation is related mainly to diffusion rather than incorporation associated with trace elements. H^+ diffusion rates may nonetheless have been affected by the zonation in the defect structure. In general, the Iki olivines contain greater concentrations of trace elements (e.g., Ti, Al, V, Cr, Zn, Li) relevant to H^+ incorporation than the San Carlos olivines.

The initial water concentration was estimated from the polarized FTIR measurements and baselines shown in Fig. 3 using both the Bell calibration and the Withers calibration and also by NanoSIMS (Table 3). These three estimates were averaged to produce initial H^+ concentration estimates of 15 ± 2 ppm H_2O in the Kilauea Iki olivine and 4 ± 1 ppm H_2O in the San Carlos olivine. These low concentrations are consistent with previous work on San Carlos (Gaetani et al., 2014). The difference in the ratio of the area when E ∥ *a* to total water concentration (Table 3) is the result of differences in the orientations of the O—H bonds between the two olivines. The H^+ concentration in the Kilauea Iki sample, for which the low rims had been polished off to prepare the sample as a rectangular parallelepiped, was homogeneous by both SIMS and FTIR.

Several different O—H absorption peaks were observed in FTIR profiles of the initial materials. The prominent

Table 3
H^+ concentration estimates for Kilauea Iki olivine and San Carlos olivine based on polarized FTIR areas (Fig. 3) and SIMS measurements.

	Kilauea Iki olivine; Kiki	San Carlos olivine; sub-samples of SC1	
FTIR area E ∥ *a* (cm^{-2})	52+/−10	7+/−5	Untreated SC1-1
		55+/−17	Partially hydrated SC1-7
		24+/−8	Partially hydrated SC1-2
		7+/−6	Dehydrated SC1-2
FTIR area E ∥ *b* (cm^{-2})	31+/−13	8+/−5	Untreated SC1-1
FTIR area E ∥ *c* (cm^{-2})	18+/−9	9+/−4	Untreated SC1-1
FTIR area summed over 3 light polarization directions (cm^{-2})	101+/−19	24+/−8	Untreated SC1-1
Water, Bell calibration (ppm H_2O)	19+/−4	4.5+/−1.5	Untreated SC1-1
Water, Withers calibration (ppm H_2O)	12+/−2	3+/−1	Untreated SC1-1
Water, SIMS (ppm H_2O)	14+/−1	5+/1	Dehydrated SC1-2
Average initial water (ppm H_2O)	15+/−2	4+/−1	SC1
Ratio of water in ppm H_2O to area in cm^{-2} with E ∥ *a*	0.3	0.6	SC1-1
Average water (ppm H_2O) after piston cylinder experiment	Not treated with pressure	32+/−23	Partially hydrated SC1-7
		14+/−10	Partially hydrated SC1-2

peaks at wavenumbers 3525 and 3573 cm^{-1} oriented primarily ‖ *a* in both Kilauea Iki and San Carlos olivine correspond to the [Ti-2H] Ti-clinohumite defect, and the high-wavenumber peaks that primarily appear as shoulders on the [Ti-2H] peaks correspond to [Si-4H] (Berry et al., 2005). A very small peak at 3600 cm^{-1} present in both samples has been ascribed to [Si-4H] with nearby Fe^{2+} (Blanchard et al., 2017). The Kilauea Iki olivine, but not the untreated San Carlos olivine, contains prominent [Fe^{3+}-H] peaks. These peaks at 3356 and 3329 cm^{-1} correspond exactly to the peak locations that Blanchard et al. (2017) associate with [Fe^{3+}-H]. No [Mg-2H] peaks were present initially in these spectra with E ‖ *a*.

3.2. Hydration

Increases in FTIR absorbance indicate that H^+ was successfully incorporated into San Carlos olivine samples SC1-7 and SC1-2 (Fig. 4A). To construct H^+ profiles, quadratic baselines were drawn to match both the curve of the spectrum of the untreated sample and the middle baselines used to determine the initial water concentration in Fig. 3. Typical baselines are illustrated in Fig. 4B and C, and all spectra and baselines are shown in the Supplement. The integrated absorbance was determined and scaled to an estimated H^+ concentration by multiplying by 0.6, following the ratio of concentration to area with E ‖ *a* reported for San Carlos olivine in Table 3.

The partially hydrated sample SC1-2 was sufficiently homogeneous for both total H^+ and individual peaks to serve as a reasonable starting material for subsequent dehydration experiments (Fig. 4). If we ignore the uncertainties associated with baseline choice and use only the quadratic baseline shown in Fig. 4C, the H^+ concentration across hydrated SC1-2 is 15 ± 1 ppm H_2O. Although there is a small increase in area around the [Fe^{3+}-H] peaks, the large majority of the H^+ in the hydrated SC1-2 is present as [Ti-2H] and [Si-4H], and these profiles are also homogeneous. This crystal was hydrated for a duration long enough to achieve the "metastable equilibrium" of Kohlstedt and Mackwell (1998). The homogeneous concentration across the crystal and its rapid rate of hydration are consistent with the results from Kohlstedt and Mackwell (1998).

In contrast, H^+ zonation is clearly observed in SC1-7, which was hydrated longer (Table 2), with central water concentrations of 38 ± 7 ppm H_2O (using the quadratic baseline shown in Fig. 4B). The intent was to enter the slower, PV stage of hydration. The variations in concentration are most apparent ‖ *c* for total H and all major peaks (Fig. 5), consistent with previously work showing *c* is the fast direction during diffusion using vacancies (the PV mechanism rate of Kohlstedt and Mackwell, 1998; Demouchy and Mackwell, 2006).

Quantifying the diffusivities in SC1-7 requires assumptions about both the solubility and metastable equilibrium concentrations. Here we assume a metastable equilibrium concentration of 15 ± 1 ppm H_2O, the observed concentration in SC1-2. This value is much higher than the 0.4 ppm H_2O (7H/10^6Si) reported by Kohlstedt and Mackwell (1998). This large difference has been difficult to reconcile

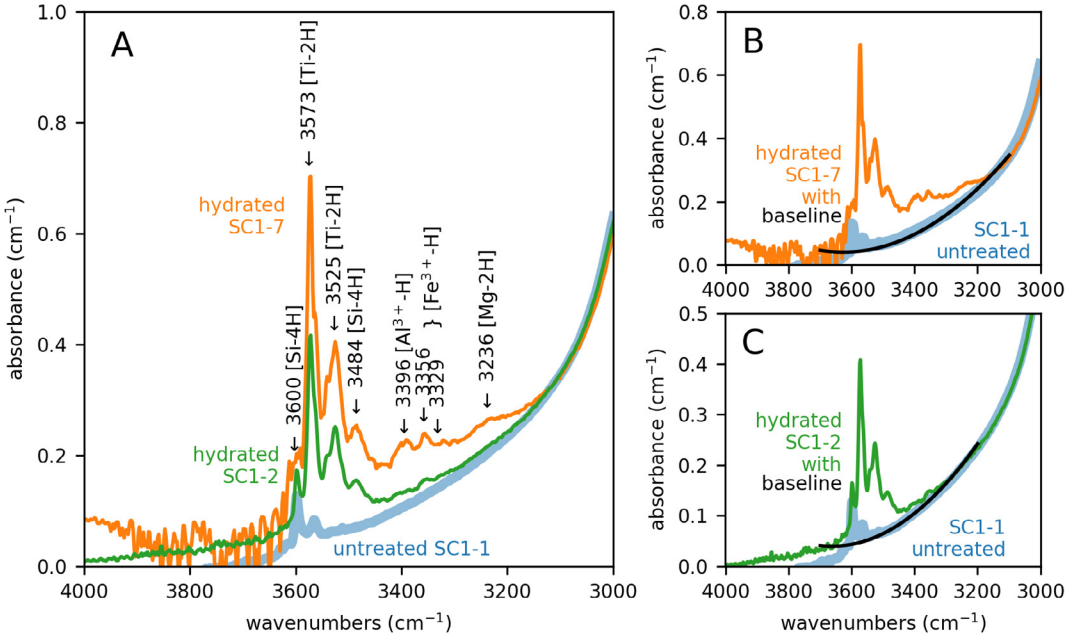

Fig. 4. (A) Polarized FTIR spectra with electric vector E ‖ *a* averaged across all traverses in three directions (see Fig. 2) of San Carlos olivine SC1 pieces that were untreated (SC1-1, blue); hydrated in a piston cylinder for exactly the amount of time (17.4 h) needed to reach metastable equilibrium at the redox rate (SC1-2, green) at 800 °C; and hydrated long enough (7 h) at 1000 °C to enter into PV-rate diffusion without saturating the sample (SC1-7, orange) with major peaks labeled. The shapes of the quadratic baselines used to calculate the areas under each curve for spectra measured are shown for SC1-7 (B) and SC1-2 (C). Note the differences in the y-axis scale. (For interpretation of the references to colour in this figure legend, the reader is referred to the web version of this article.)

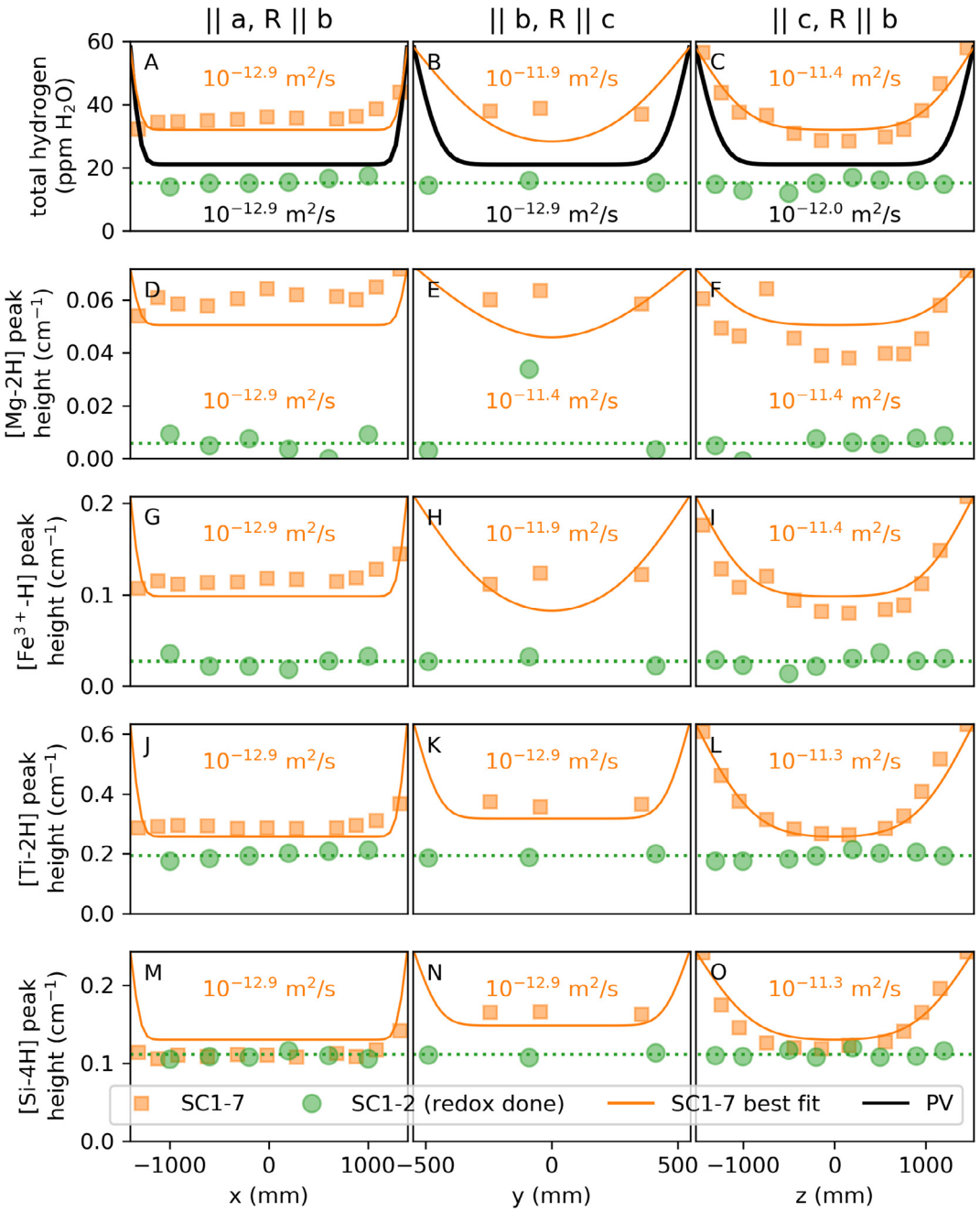

Fig. 5. Concentration profiles across San Carlos olivine samples SC1-2 and SC1-7 after partial hydration in a piston cylinder as measured through the uncut block. R is the ray path of the infrared beam, and the electric vector E of the polarized beam is in all cases || *a*. H^+ concentrations are estimated from polarized FTIR spectra using the areas under the baselines shown in Fig. 3 and initial H^+ contents from Table 2. Black numbers and curves show the expected diffusion curves based on the diffusivities (D) for proton-vacancy (PV) rate diffusion at 1000 °C, an initial metastable equilibrium concentration equal to the mean concentration or peak height in the hydrated SC1-2 (dotted green lines, where all diffusion possible by the proton-polaron (redox) mechanism has been completed) and final concentration of 58 ppm H_2O. Thin orange lines show curves for the reported diffusivities, assuming the same initial and final concentration as the PV lines. The large difference between the black and orange curves in panel A despite their having the same diffusivity is a result of path integration effects along the ray path, *b*, which has significantly different diffusivities for the two models. See Ferriss et al. (2015) for a more complete discussion of this "whole-block" effect. (For interpretation of the references to colour in this figure legend, the reader is referred to the web version of this article.)

but may be related in part to differences in the Fe^{3+} content and/or the calibrations used to determine H^+ concentrations from FTIR spectra in the two studies. The accepted values for the PV rate (Demouchy and Mackwell, 2006) fit our data reasonably well if we assume a final solubility of 150 ppm H_2O, which is possible, particularly given the

still large uncertainties in the solubility of H^+ in olivine (Mosenfelder et al., 2006; Zhao et al., 2004; Tollan et al., 2017). Fig. 5 shows the best fit to our whole-block SC1-7 data that assumes a final concentration equal to the maximum observed rim concentration of 58 ppm H_2O. This fit requires diffusivities that are slightly higher along the fast *c*-direction (~ 0.5 log unit), significantly higher ‖ *b* (1 log unit), and comparable ‖ *a* to those reported by Demouchy and Mackwell's (2006) for their PV mechanism. Diffusivities higher along *b* than *c* are unexpected but not entirely without precedent (e.g., Demouchy and Mackwell, 2003; Demouchy et al., 2016) and not well constrained here by only three interior points.

3.3. Dehydration

SC1-2 and Kiki, two homogeneous blocks of olivine with similar initial starting H^+ concentrations but very different histories, compositions, and distributions of H^+, were sequentially dehydrated in a gas-mixing furnace (Fig. 6). The choice of baseline is well known as a major source of error in FTIR analyses, and associated errors in the resulting peak heights and areas may be as high as 30%, consistent across profiles. All profiles were normalized to a relatively homogeneous starting profile. While this error due to baseline selection is very large, it is a consistent offset for all estimates that is mostly eliminated by dividing by the initial values, which contain the same systemic error related to baseline choice. Path-integrated 3-dimensional diffusion modeling was then performed on each profile to estimate the rate of H^+ mobility and associated errors after each heating step (see Supplemental material). These efforts are described in more detail for each sample in the sections below. Most of the resulting diffusivities (see Supplemental Table) show H^+ loss rates that are *intermediate* between the redox and PV rates.

3.3.1. Dehydration of San Carlos olivine

We determined H^+ loss curves and diffusivities for total H^+, [Si-4H] at 3600 cm^{-1}, and [Ti-2H] at 3525 cm^{-1} in San Carlos SC1-2. All spectra, baselines, profile data, and best-fit curves are provided in the Supplemental PDF. Selected profile data are shown in comparison with expected redox rate profiles in Fig. 7, and all estimated diffusivities are shown as a function of annealing time in Fig. 8.

The height of the [Si-4H] peak clearly decreases more slowly than the rest of the peaks and did not decrease in height during the first 5 heating steps at 800 °C. After 43 h, when the large majority of the initial H^+ had left the crystal and the bulk of the remaining H^+ was present in the [Si-4H peak], clear H^+-loss profiles could be observed for [Si-4H], with apparent diffusivities that were relatively fast compared to the initial stages and with a fast direction of diffusion ‖ *a*. These [Si-4H] loss profiles also differ from the majority of profiles observed in this study in that they did not decrease to zero near the edges, but rather to about 40% of the initial concentration, which was the final concentration used when modeling the diffusivities. Over the

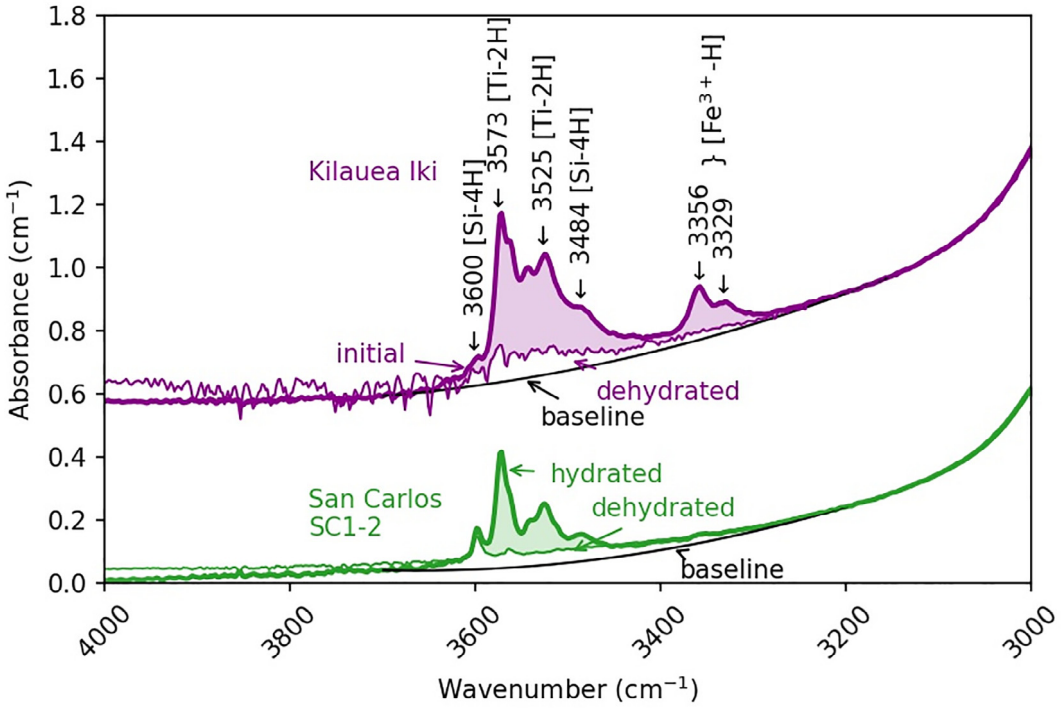

Fig. 6. Averaged polarized FTIR spectra with electric vector E ‖ *a* of Kilauea Iki olivine (offset for clarity) and partially hydrated San Carlos olivine SC1-2 before and after heating in a gas-mixing furnace and normalized to 1-cm thickness.

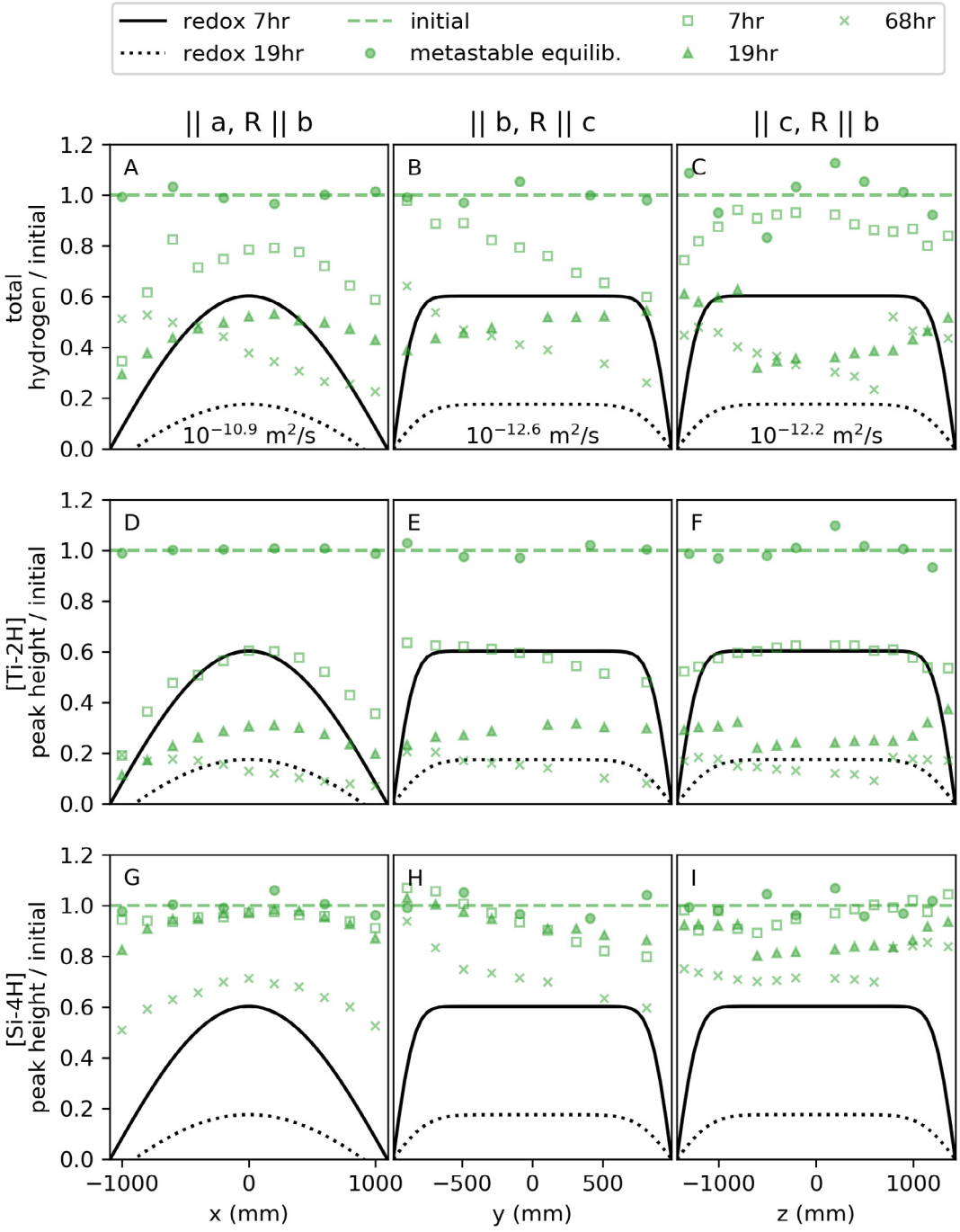

Fig. 7. Path-integrated profiles of (A–C) total H, (D–F) the Ti-clinohumite [Ti-2H] peak at 3525 cm^{-1}, and (G–I) the [Si-4H] peak at 3600 cm^{-1} during step-wise dehydration of an uncut block of partially hydrated San Carlos olivine SC1-2 at 1 atm, 800 °C, and NNO-2.6. R is the ray path of the infrared beam. All data are normalized to a best-fit line through the hydrated profile data to account for small amounts of initial zonation. Black lines show expected hydrogen loss curves at the redox rate (diffusivities labeled in A–C). The redox rate is somewhat too fast to describe the total H data and much too fast to describe the [Si-4H] peak data. The [Ti-2H] data is very well described by the redox rate after 7 h of heating, but [Ti-2H] movement slows down by 19 h. Baselines and best-fit diffusivities and curves are provided in the Supplemental PDF.

course of the final heating steps, the rate of [Si-4H] mobility increased noticeably, from $10^{-12.6}$ m^2/s at 19 h to $10^{-11.8}$ m^2/s ‖ *a* at 68 h.

While the decrease in the height of the [Si-4H] peak accelerated during the experiment, the loss of H^+ from the [Ti-2H] peak slowed down. To observe this decrease in H^+ loss rate in the profile data, compare the close correspondence of the [Ti-2H] data with the expected redox rate curves at 7 h with the large difference between the data and the redox curves at 19 h (Fig. 7D–F). The [Si-4H] and

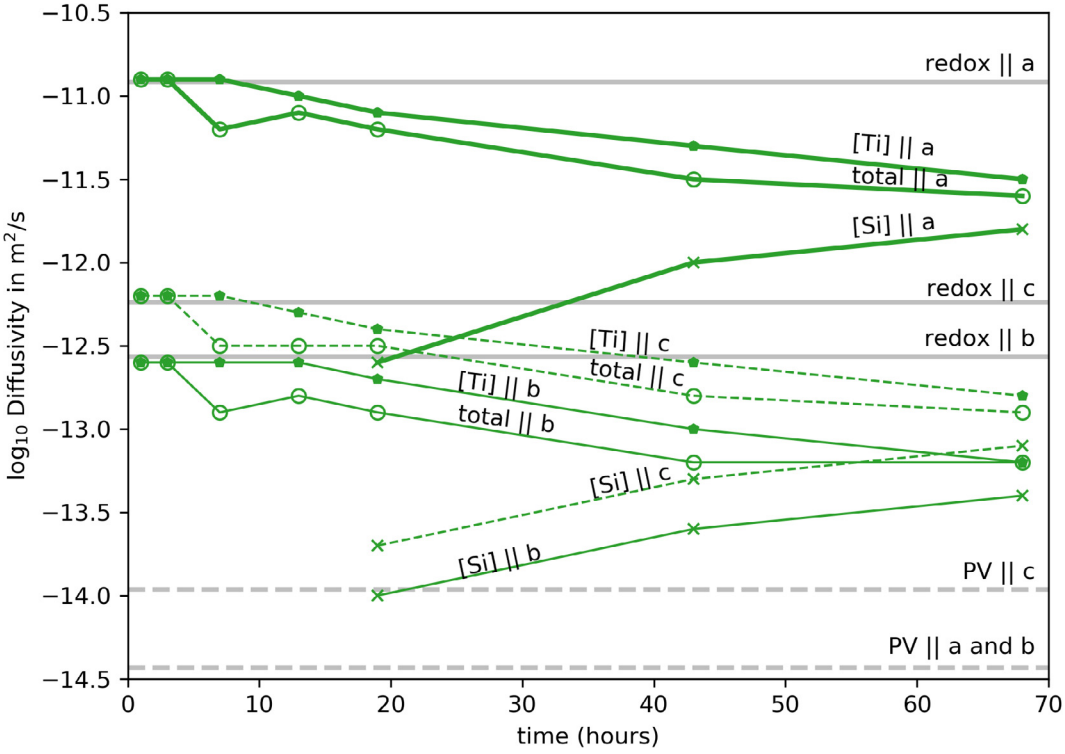

Fig. 8. Estimated rates of H^+ movement represented as diffusivities in San Carlos olivine SC1-2 with heating time at 800 °C and oxygen fugacity of $10^{-16.5}$ bars (NNO-2.6) in three crystallographic directions for total H^+ and two peak-specific mechanisms described in the text, [Si-4H] and [Ti-2H], compared with expected diffusivities for the proton-vacancy (PV) and redox rates. Errors on all diffusivities (provided in Supplement) are omitted for clarity. The anisotropy of the observed diffusivities and redox is similar, with movement $\| a > c > b$, but the exact values are not consistent over time. At early heating stages, the total H^+, which is dominated by the mechanism [Ti-2H], is consistent with expected redox values, but over time those diffusivities decrease. In contrast, the [Si-4H] mechanism is initially too slow to be measured confidently, but after 19 h enough movement could be observed for fitting. These [Si-4H] diffusivities increased at 43 and 68 h, approaching the values for [Ti-2H] and total H. The profile data used to obtain these diffusivities are shown in Fig. 7 and the Supplement.

[Ti-2H] diffusivities come close to converging, but the [Ti-2H] peak diffusivity is always higher (Fig. 8). Profiles for the other [Ti-2H] peak (3575 cm^{-1}) and additional [Si-4H] peaks in SC1-2 are not shown but behave similarly to [Ti-2H] (3525 cm^{-1}).

The total H^+ curves, which consist of a combination of peaks, the [Si-4H] and [Ti-2H] peaks, show apparent diffusivities that are intermediate between the final [Ti-2H] and [Si-4H] mechanism diffusivities. For the final two experiments at 43 and 68 h, the observed diffusivity for the total H is within 0.1 log units of the arithmetic mean of the [Si-4H] and [Ti-2H] diffusivities. In the 19 h data, the observed total H diffusivities are slightly higher, 0.1–0.2 log units, than would be expected from the mean of the [Ti-H] and [Si-4H] diffusivities, suggesting that H^+ is exiting the crystal from additional mechanism(s). This relationship is less clear at shorter times because there is so much uncertainty in the [Si-4H] diffusivities. The total H^+ curves are also typically less symmetric than the profiles of either the [Ti-2H] or [Si-4H] peak, in part because of the occasional appearance of spectra with relatively large [Fe^{3+}-H] peaks and distorted baselines (see Supplemental PDF, e.g., 100 μm from the edge along *a* after 43 h of heat treatment). This [Fe^{3+}-H] peak appeared intermittently near all edges of SC1-2 frequently enough that it is unlikely to be contamination but too infrequently to model with confidence. The final total H^+ concentration was modeled using 15% of the initial homogeneous partially hydrated concentration because the [Si-4H] peak does not decrease to zero at the rim (as noted above), and therefore the total H^+ also cannot go to zero. During the initial dehydration stages, when the [Si-4H] peak at 3600 cm^{-1} was a relatively minor component, the total H^+ could be modeled well with the redox rate, similar to [Ti-2H]. By the end of the experiment, the total H^+ diffusivity had dropped from $10^{-10.9}$ to $10^{-11.6}$ $m^2/s \| a$.

3.3.2. Experimental dehydration of Kilauea Iki olivine

Experimentation on the Kilauea Iki sample took place in two stages. First, the sample was treated exactly the same way as SC1-2 during dehydration: heated at 800 °C in a gas-mixing furnace at NNO-2.6. Second, the sample was sequentially heated at 1000 °C, largely at NNO-2.6 (for 3, 6 and 7 total hrs) and then at NNO + 1.9 for a final increment at 8 total hours. Heating the Kilauea Iki sample at 800 °C for 8 h did not produce any clear loss in total H or [Ti-2H] (Fig. 9). Although total H^+ and [Ti-2H] did not change, heating the Kilauea Iki olivine at 800 °C did result in significant re-organization, where the H^+ from [Fe^{3+}-H] decreased by 50% and the H from [Si-4H]

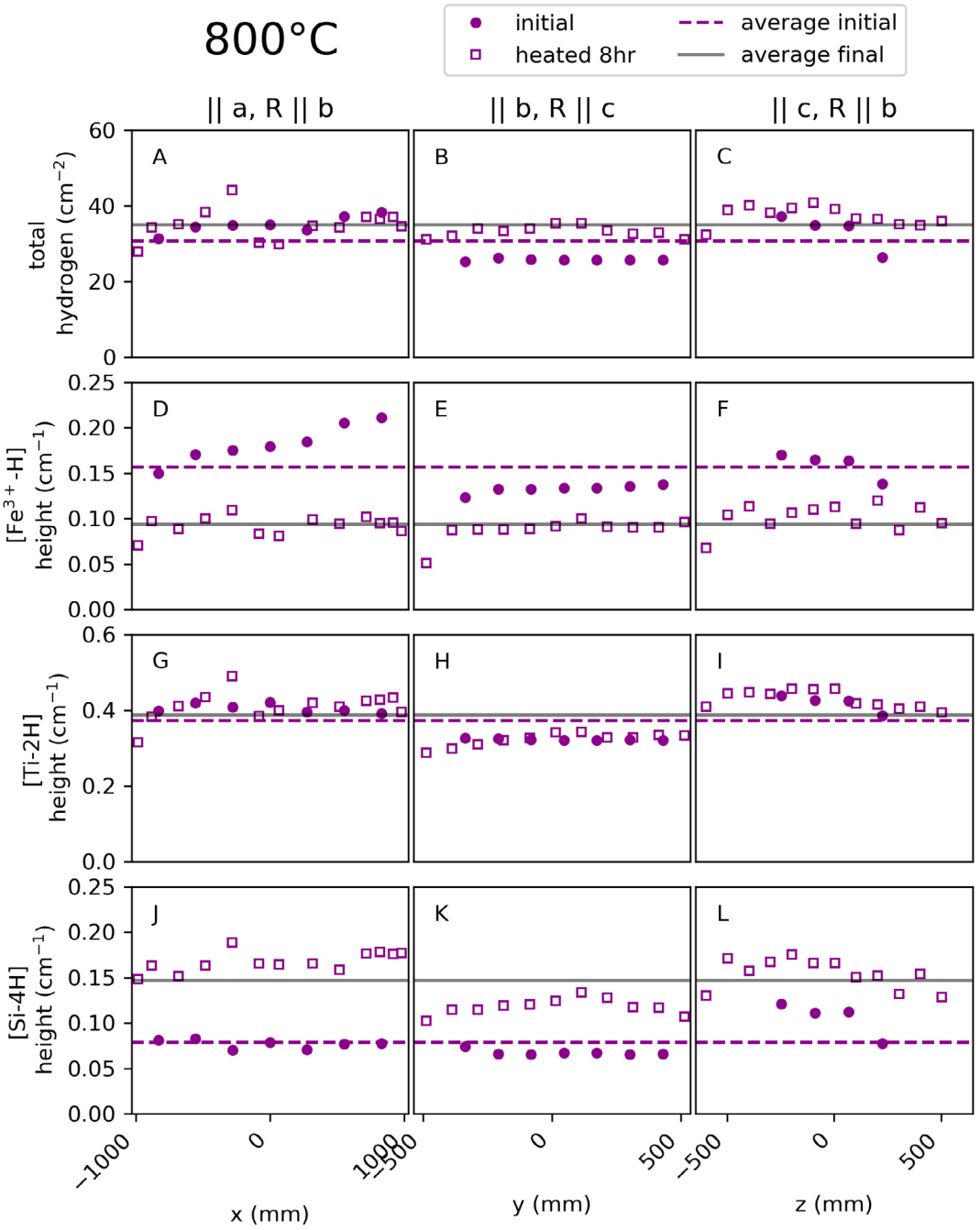

Fig. 9. Path-integrated profiles of (A–C) total H^+, (D–F) the [Fe^{3+}-H] peak at 3356 cm^{-1}, (G–I) the [Ti-2H] peak at 3525 cm^{-1}, and (J–L) the [Si-4H] peak at 3600 cm^{-1} in an uncut block of Kilauea Iki olivine after 8 h of heating at 1 atm and 800 °C. R is the ray path of the infrared beam. The increase in the average [Si-4H] peak height of 0.06 cm^{-1} is similar to the decrease in the average peak height of the [Fe^{3+}-H] peak. The apparent increase of 4 ppm H_2O in the total H^+ is small enough (15% change) to be within error of the initial.

doubled. The Kilauea Iki 800 °C [Fe^{3+}-H] loss on reorganization rates were initially fast, around $10^{-11.0}$ m^2/s || *c* at 1 hour before dropping to $10^{-12.5}$ m^2/s at 8 h. This drop in the [Fe^{3+}-H] mobility rate suggests that the large majority of the internal H^+ reorganization had been completed. The relative flatness of all of the profiles suggests that the movement was occurring everywhere throughout the crystal simultaneously, consistent with reorganization. The profiles from these 8 h of heating at 800 °C were used as the 'initial' profiles for data collected during a second stage of heating at a higher temperature.

The heating temperature was raised to 1000 °C because the maximum total H^+ diffusivities observed at 800 °C were unlikely to produce clear H^+ loss profiles within laboratory time scales. The oxygen fugacity was maintained along the same buffer curve, NNO-2.6, for 3 heating steps totaling 3,

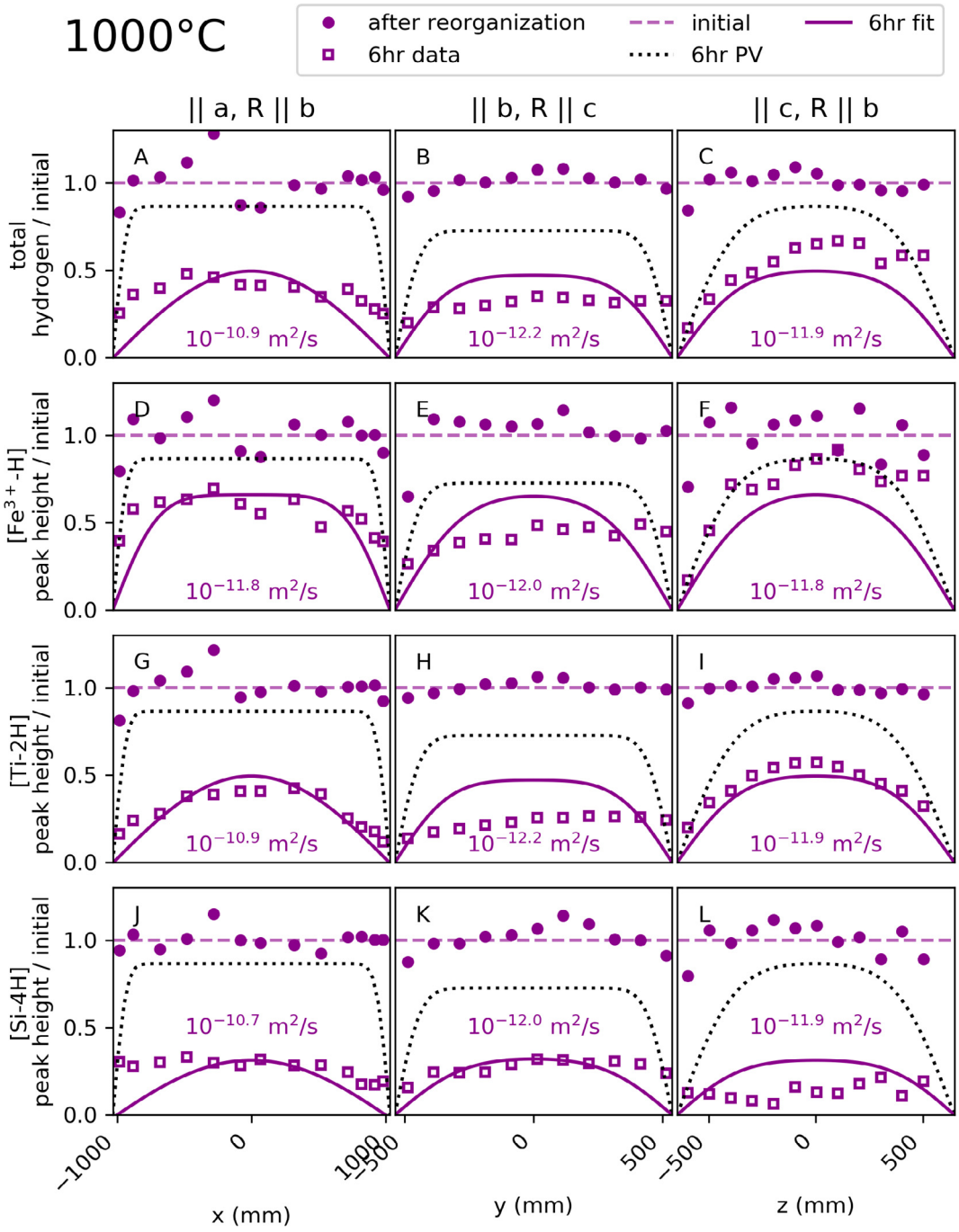

Fig. 10. Path-integrated profiles of (A–C) total H^+, (D–F) the [Fe^{3+}-H] peak at 3356 cm^{-1}, (G–I) the [Ti-2H] peak at 3525 cm^{-1}, and (J–L) the [Si-4H] peak at 3600 cm^{-1} in an uncut block of Kilauea Iki olivine after 6 h of heating at 1 atm and 1000 °C. R is the ray path of the infrared beam. All profiles are normalized to profile data measured after heating for 8 h at 1 atm, 800 °C, and NNO-2.6, which produced significant re-organization of the hydrogen across different sites (Fig. 8). Numbers are the diffusivities that correspond to the purple lines fit to the data. The proton-vacancy rate (PV, dotted lines) is too slow to account for all of the observed H^+ movement. If H^+ were decreasing at the proton-polaron rate, redox, then all H^+ would have been lost from the crystal. Baselines and best-fit diffusivities and curves are provided in the Supplement. Note the differences in x-axis scales and that this data is measured through the uncut block, and therefore measurements in the center of each profile may differ along different ray paths.

6, and 7 h, and in each of these steps, the rate of H^+ loss could be estimated as $10^{-10.9}$ m^2/s for total H^+ and [Ti-2H] and $10^{-10.7}$ m^2/s for [Si-4H] parallel to the fast direction *a*. These fits are shown in Fig. 10 for 6 h of annealing, and the other concentration profiles are provided in the Supplement. The [Si-4H] loss profiles in Kilauea Iki (Fig. 10J–L), unlike in San Carlos (Fig. 7G–I), appear to decrease to zero concentration at the rim, and to decrease

at a rate faster than [Ti-2H]. The [Fe^{3+}-H] loss at 1000 °C was slower than the other peaks and did not include an obvious fast direction of diffusion at this temperature of annealing.

A final heating step of 1 additional hour was performed for a total of 8 h heating at 1000 °C under more oxidizing conditions, NNO + 1.9. The resulting loss of H^+ for all mechanisms was consistent with the diffusivities determined under more reducing conditions, which suggests that the role of oxygen fugacity has little effect on the diffusivities, at least for this very late stage of dehydration and over such a short duration (1 h).

3.4. Total H^+ diffusivity in Kilauea Iki olivine during ascent

SIMS analysis of Kikin, the natural Kilauea Iki olivine phenocryst, along its crystallographic *a* axis indicates a central H^+ concentration of ~9 ppm H_2O, decreasing to concentrations of ~6 ppm at the crystal edges (Fig. 11). The H^+ concentration gradients recorded in the outer ~200 μm of the crystal are suggestive of syneruptive water loss from the olivine in response to degassing of the host magma on ascent. Unlike the profile along *a*, the profile measured along *c* exhibits a constant H^+ concentration. No decrease in H^+ concentration was detected at the edge of the crystal along the *c* axis, suggesting that any signature of syneruptive degassing along the *c* direction may be confined to the region <~20 μm from the edge of the crystal, i.e., not resolvable at the spatial resolution of our analyses. These observations thus indicate that this crystal experienced greater loss of H^+ parallel to *a* than parallel to *c*.

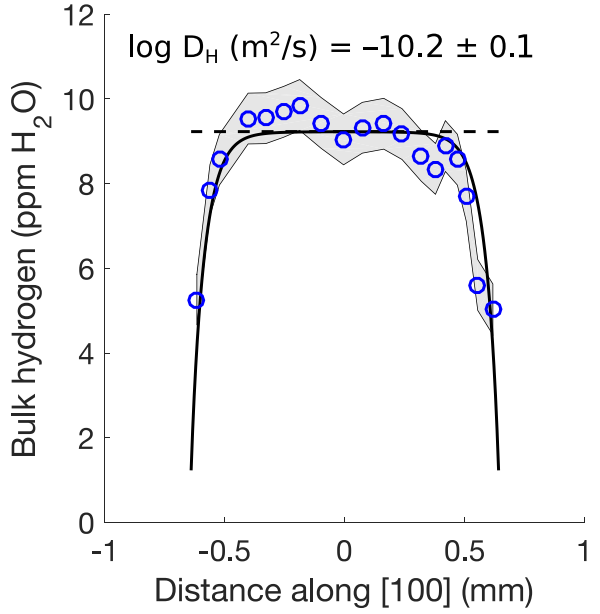

Fig. 11. SIMS measurements of total H^+ along *a* in a Kilauea Iki olivine phenocryst and best-fit diffusivity at 1192 °C based on Monte Carlo modeling and a 1D diffusion model. The grey envelope shows the data plus/minus 2 standard deviations, which is 0.6 ppm H_2O.

The plateau in H^+ concentration along *a* (the apparent fast direction) supports our use of a 1D model, the results of which indicate a trade-off between D and K_d, with higher best-fit values of K_d resulting in higher best-fit values of D. No clear trade-off is observed between best-fit values of D and dP/dt. Our Monte-Carlo simulation suggests a H^+ diffusivity ‖ *a* of $10^{-10.17+/-0.08}$ m^2/s at the temperature 1192 °C determined by Ferguson et al. (2016).

3.5. Estimated total H diffusivity during dehydration of natural olivine

Although the treated crystals show some complex phenomena, such as rapid reorganization of peaks and rate changes with time, the H^+ diffusivities determined at the end of each experiment, (i.e., the data in San Carlos olivine SC1-2 after 68 h of heating at 800 °C and in the Kilauea Iki olivine after 8 h of heating at 1000 °C) and the diffusivity ‖ *a* for the untreated Kilauea Iki olivine at 1200 °C form a remarkably consistent Arrhenius relationship (Fig. 12). This result is surprising, given that different defect structures typically result in different defect formation energies and hence different Arrhenius laws. In the discussion we explore some reasons why H^+ diffusivities in different olivines may converge and the coherence of other experimental data to this working Arrhenius law.

We estimate common Arrhenius laws for total H^+ in natural Fe-bearing olivine in all three directions during dehydration for potential use in applications such as ascent modeling. For convenience, the activation energy is assumed to be 130 kJ/mol and constant for all three directions. This activation energy was determined by fitting the data ‖ *a*, and then the same activation energy was used ‖ *b* and ‖ *c*, the directions for which only 2 data points are available. The pre-exponential factor D_0 was then determined for each direction as follows: $10^{-5.4}$ m^2/s ‖ *a*, $10^{-6.9}$ m^2/s ‖ *b*, and $10^{-6.6}$ m^2/s ‖ *c*. The final diffusivity estimates for [Ti-2H] and [Si-4H] are similar to those for total H^+ and so are likely to follow similar Arrhenius laws.

The errors on these Arrhenius laws are difficult to estimate with only 2–3 data points in each line, and additional data, particularly at high temperatures, would be very welcome. There is also no compelling reason to expect the activation energy to be constant for different olivines or different directions, and we expect future studies to explore and quantify these differences. In the meantime, the Arrhenius laws in Fig. 12 should provide useful initial estimates.

4. DISCUSSION

4.1. Overview of changes in the defect structures

Our results suggest that in addition to driving H^+ in or out of the structure, the energetic stability of a hydrated olivine may in some cases be increased by a redistribution of the H^+ among different H^+ storage sites. H^+ redistribution can be seen in both the San Carlos olivine (i.e., the coupled slowing down of the rate of [Ti-2H] loss with the speeding up of [Si-4H] loss) and Kilauea Iki olivine (i.e., the coupled increase in [Si-4H] with a decrease in [Fe^{3+}-H]). Our goal in

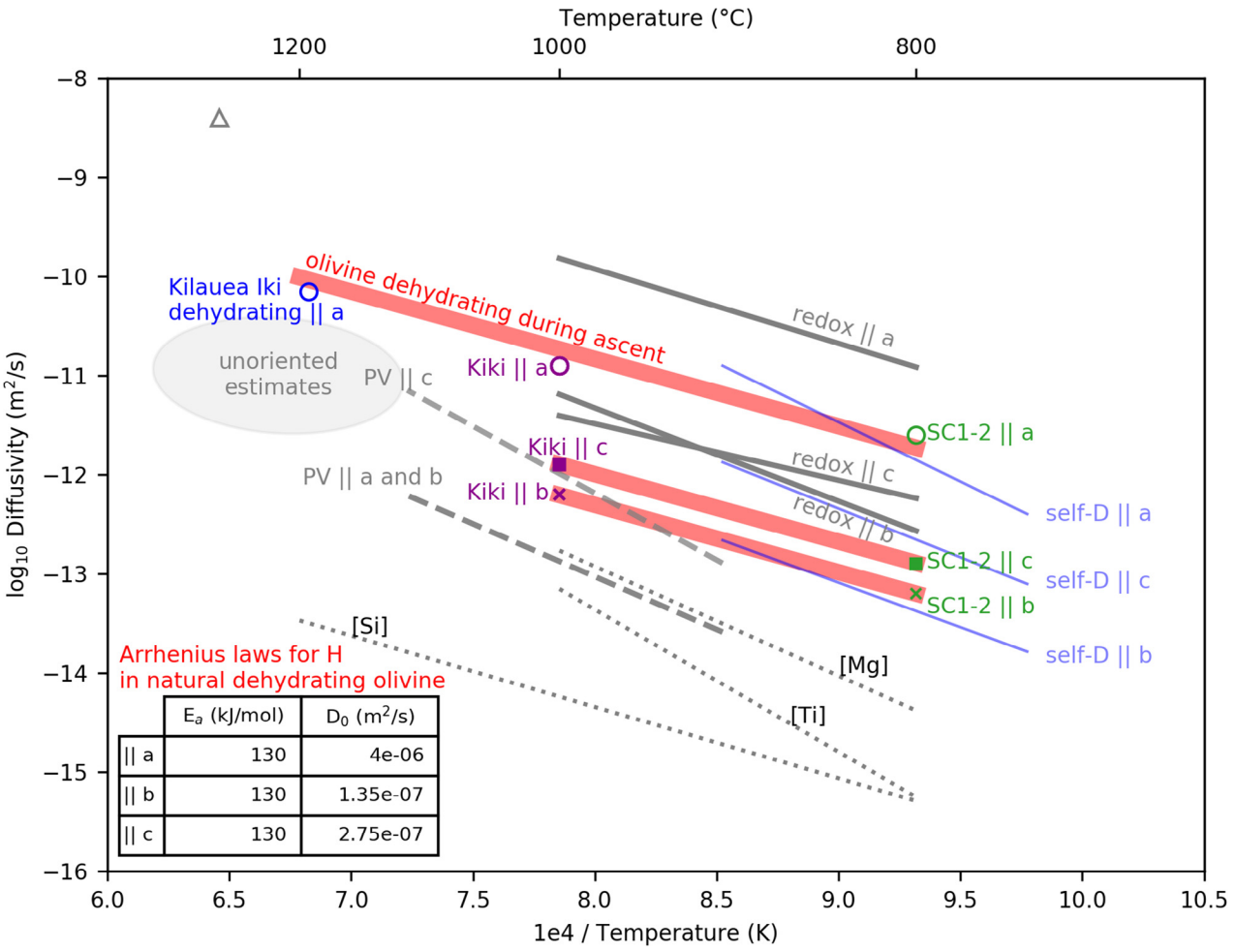

Fig. 12. Arrhenius diagram for the rate of total H^+ movement in olivine. Grey lines show ranges for previous measurements of the proton-polaron rate (redox; solid lines) and the proton-vacancy rate (PV; dashed lines) during hydration of San Carlos olivine (Kohlstedt and Mackwell, 1998; Demouchy and Mackwell, 2006) as well as peak-specific measurements from the dehydration of synthetic forsterite (dotted lines, Padrón-Navarta et al., 2014). Blue lines show estimated H self-diffusivities based on H-D exchange in partially hydrated San Carlos olivine (Du Frane and Tyburczy, 2012; Novella et al., 2017). Thick pink lines show fits through the final observed total H^+ diffusivity measurements from this study: the experimental dehydration of San Carlos olivine at 800 °C (SC1-2, green), the experimental dehydration of Kilauea Iki olivine at 1000 °C (Kiki, purple), and the estimated diffusivity in Kilauea Iki || *a* during its ascent at 1200 °C (blue circle). Six out of seven independent estimates for total H diffusivity in unoriented melt-inclusion-bearing olivines (gray circled area that includes 1 diffusivity from Portnyagin et al., 2008; Mironov et al., 2015; 4 diffusivities from Chen et al., 2011; and 1 diffusivity from Gaetani et al., 2012) fall between and so are consistent with these fits. The exception is a higher diffusivity estimate by Hauri (2002) for an olivine from Loihi (grey triangle). The activation energies (E_a) and pre-exponential factors (D_0) for our fits are provided in the inset table. An interactive Arrhenius diagram that includes additional measurements and all time-series and peak-specific data is available in an online app https://arrheniusdiagram.herokuapp.com. (For interpretation of the references to colour in this figure legend, the reader is referred to the web version of this article.)

the next two discussion sections is to provide relatively simple, possible explanations for these observed changes in the H^+ defect concentrations based on the defects listed in Table 1. Future research may well suggest alternate explanations or indicate that some other defects, e.g., those involving phosphorous, should also be considered.

4.2. Defect evolution during hydration and dehydration San Carlos olivine

Fig. 13 illustrates our inferred evolution of H-defects during hydration and then dehydration of our single block of San Carlos olivine, SC1-2. We developed this inferred evolution by attempting to explain the observed changes in FTIR peaks while satisfying three major constraints. First, the fact that H^+ is able to enter San Carlos olivine so quickly suggests that only hydrogen (as protons) and/or electrons are moving because the diffusion of metals and vacancies is too slow to accommodate such rapid hydration (Mackwell and Kohlstedt, 1990). Second, the H^+ is incorporated primarily as [Ti-2H], which involves Ti on the octahedral site (Walker et al., 2007). Third, anhydrous Si vacancies are generally unfavorable in olivine (Houlier et al., 1990).

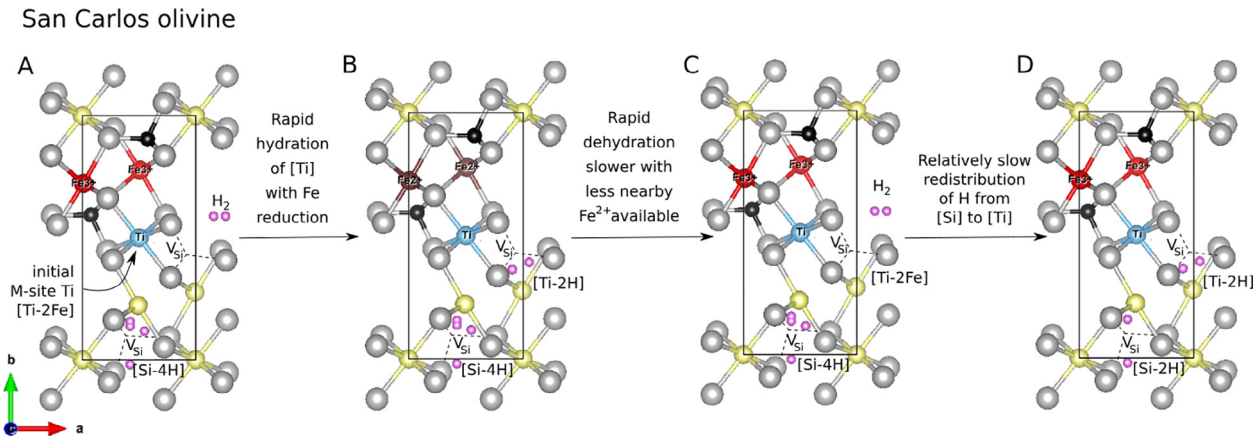

Fig. 13. Crystal models of olivine viewed down the *c* axis to illustrate defects in San Carlos olivine (A) prior to treatment, (B) after hydration in a piston cylinder, (C) after the rapid initial stages of dehydration in a gas-mixing furnace, and (D) after continued heating resulting in partial redistribution of H^+. Defect labels are explained in Table 1. Ball colors corresponds to the following: yellow is Mg; grey is O; black is Si; blue is Ti, pink is H, red is Fe^{3+}, and brown is Fe^{2+}. H positions and the substitution of Ti on an M1 site were selected following Walker et al. (2007) but are intended to provide a simple illustration of the reactions described in Eqs. (2) and (4), not to show definitive locations for all atoms in the structure. Crystal images were created using VESTA (Momma and Izumi, 2011). (For interpretation of the references to colour in this figure legend, the reader is referred to the web version of this article.)

Panels 13A to 13B show rapid hydration, which affected primarily [Ti-2H] and occurred at the redox rate, with a fast direction ‖ *a*. This rapid influx of H^+ indicates that the defect structure must have already been favorable to a redox mechanism of hydration. Given that [Ti-2H] was the dominant defect that was formed at the redox rate, the likely initial defect structure must have included Ti already present in the octahedral site with nearby Fe^{3+} to create charge balance with the associated Si vacancy. Such [Ti-Fe^{3+}] defects are primed for rapid hydration, with H_2 supplying the electrons needed to reduce the $2Fe^{3+}$ to $2Fe^{2+}$, forming protons that then create [Ti-2H]. This reaction may be described broadly for hydration (Fig. 13A → B) as

$$\left[\mathrm{Ti}-2\mathrm{Fe}^{3+}\right]+\mathrm{H}_2\rightarrow[\mathrm{Ti}-2\mathrm{H}]+2\mathrm{Fe}^{2+} \tag{2a}$$

in Kröger-Vink notation as

$$\{Ti^{\bullet\bullet}-V''''_{Si}-2Fe^{\bullet}_{M}\}+2O^{x}_{O}+H_2 \rightarrow \{Ti^{\bullet\bullet}-V''''_{Si}-2OH^{\bullet}_{O}\}+2Fe^{x}_{m} \tag{2b}$$

and in terms of olivine formula units as

$$\mathrm{MgTiFe_2SiO_8}+\mathrm{H_2}\rightarrow\mathrm{MgTiH_2O_4}+\mathrm{Fe_2SiO_4} \tag{2c}$$

Eq. (2) could also be written in terms of the related chemical species H_2O and O_2 instead of H_2. Here we use H_2 mainly for simplicity and consistency with previous work (e.g., Mackwell and Kohlstedt, 1990), but the formation of a small neutral species is also appealing in that it may at least partially explain the rapid movement of the hydrogen because the diffusion of a neutral species does not require any accompanying charge transfer.

The primary difficulty with Eq. (2) is that it requires that the [Ti-2Fe^{3+}] defect be present initially, and octahedral Ti is not typically present in anhydrous olivine. One possible alternative to Eq. (2) was suggested by Padrón-Navarta et al. (2014) in their Eq. (6): $Mg_2TiO_4 + H_2O \rightarrow MgTiH_2O_4 + ½\ Mg_2H_4O_4$, but this reaction requires the movement of Ti from an octahedral site to a tetrahedral site over hour times scales, at rates comparable to PP. Whether such movement is possible would depend on the diffusivity of Ti, which is far too low to accommodate PP-rate diffusion (Cherniak and Liang, 2014), the diffusivity of Mg vacancies, which is higher than Ti vacancies but still much lower than the redox rate (Nakamura and Schmalzried, 1984; Mackwell et al., 1988), and having a high enough concentration of nearby metal vacancies, which is difficult to measure.

The presence of octahedral Ti in San Carlos olivine may be explained by slow hydration incorporation reactions that result in the transfer of Ti from tetrahedral to octahedral sites having occurred previously at high temperature, followed by rapid dehydration and cooling over hours in a lava flow. The Ti would then be locked into the octahedral site. The geological occurrence of our San Carlos olivine is unknown in detail, but likely derives from one of the large xenoliths hosted in San Carlos lavas. Such rapid cooling would have exploited the same kind of redox mechanism in moving from 13A to 13B, but in reverse. Thus, any rapid influx of H^+ at the redox rate into an olivine may be limited not only by the initial quantity of Fe^{3+} (Kohlstedt and Mackwell, 1998) but the initial amount of Ti, and perhaps specifically octahedral Ti. Such a process is sometimes referred to as rapid "decoration" of existing defects. In this case, the initial octahedral Ti defects were likely created during cooling in a lava flow.

Panels 13B to 13C illustrate the initial, rapid dehydration of the same San Carlos SC1-2 block that had just been hydrated rapidly. The initial dehydration was manifest entirely in a decrease in the [Ti-2H] peak, once again at the redox rate, with a fast direction ‖ *a* (Fig. 7D). This dehydration can be viewed as a reversal of the redox-mediated hydration that had just occurred (which was itself a reversal of redox-mediated dehydration that had occurred in nature,

during post-eruptive cooling of the San Carlos olivine). The [Ti-2H] defects that had just formed were favorable for rapid dehydration, as $2H^+$ gained electrons from nearby Fe^{2+}, oxidizing the Fe once again. The reactions can be written as Eqs. (2a)–(2c) in reverse. Most of the [Si-4H] peaks behaved similarly to [Ti-2H], with the exception of one small peak at 3600 cm^{-1} (Fig. 6).

After 19 h, the intensity of the [Si-4H] peak at 3600 cm^{-1} also started to decrease, as the rate of decrease in the [Ti-2H] peak intensity slowed (Fig. 8). The coupled rate changes in these peak intensities suggest that at least some of the H^+ leaving [Si-4H] is doing so by moving into Si vacancies associated with [Ti-2H] rather than leaving the crystal directly. Panels 13C to 13D illustrate this reorganization of H^+, moving from [Si-4H] to [Ti-2H]. The [Ti-2H] mechanism is known from incorporation studies as a particularly favorable position for H^+ (e.g., Berry et al., 2005). Because of the energetic favorability of [Ti-2H] relative to other H^+ charge-balance mechanisms (Walker et al., 2007), any H^+ that is unable to leave readily by redox from [Si-4H] may prefer to move into recently-vacated Si vacancies that bring it closer to the octahedral Ti. This redistribution of H^+ between sites may be described by the following equation, which is illustrated in Fig. 13 C → D:

$$\left[\mathrm{Ti}-2\mathrm{Fe}^{3+}\right]+[\mathrm{Si}-4\mathrm{H}]\rightarrow[\mathrm{Ti}-2\mathrm{H}]+[\mathrm{Si}-2\mathrm{H}] \quad (3a)$$

Eq. (3) may be described in Kröger-Vink notation as

$$\left\{Ti^{\bullet\bullet}-V''''_{Si}-2Fe^{\bullet}_{M}\right\}+\left\{V''''_{Si}-4OH^{\bullet}_{O}\right\}\rightarrow\left\{Ti^{\bullet\bullet}-V''''_{Si}-2OH^{\bullet}_{O}\right\}+\left\{2Fe^{\bullet}_{M}-V''''_{Si}-2OH^{\bullet}_{O}\right\} \quad (3b)$$

and in terms of olivine formula units as

$$\mathrm{MgTiFe_2SiO_8}+\mathrm{Mg_2H_4O_4}\rightarrow\mathrm{MgTiH_2O_4}+\mathrm{Fe_2H_2O_4}+\mathrm{Mg_2SiO_4} \quad (3c)$$

The coupling of H^+ loss from [Ti-2H] with its gain from [Si-4H] may explain both the observed change in apparent diffusivities (Fig. 8) and the possibility of buffering or reaching a steady state in the overall rate of total H^+ loss, which may be set by the rate at which H^+ redistributes between [Si-4H] and [Ti-2H]. The H^+ leaves quickly from [Ti-2H] at the redox rate throughout the duration of the experiment, but the peak appears to slow down as more and more H^+ moves into [Ti-2H] from [Si-4H]. Thus, the observed loss of the [Si-4H] peak may not represent H^+ moving out of the sample at all, but rather may indicate the rate at which the H^+ is redistributing between sites. As the slower rate, the redistribution rate between [Si-4H] and [Ti-2H] may set the total loss of H^+ from the San Carlos. This redistribution is slow enough to observe over a period of days because this experiment was conducted at the relatively low temperature of 800 °C, but at magmatic temperatures and/or in samples with higher concentrations of H^+ in relatively unstable defects, the redistribution rates are likely to be higher. The coupling of rates, and potential for steady state, can be seen by coupling the reverse of Eq. (2) with Eq. (3):

$$[\mathrm{Ti}-2\mathrm{H}]+2\mathrm{Fe}^{2+}\rightarrow\left[\mathrm{Ti}-2\mathrm{Fe}^{3+}\right]+\mathrm{H_2} \quad (2arev)$$

$$\left[\mathrm{Ti}-2\mathrm{Fe}^{3+}\right]+[\mathrm{Si}-4\mathrm{H}]\rightarrow[\mathrm{Ti}-2\mathrm{H}]+[\mathrm{Si}-2\mathrm{H}] \quad (3a)$$

As H^+ loss proceeds at the redox rate from [Ti-2H], the number of anhydrous Si vacancies associated with [Ti-$2Fe^{3+}$] increases, and so the redistribution of H^+ from [Si-4H] to [Ti-2H] becomes easier and thus faster. Although the rate of [Si-4H] loss increased, the intensity of the [Si-4H] peak at 3600 cm^{-1} never reached zero, which suggested that the Si vacancies were never completely dehydrated, consistent with work suggesting that anhydrous Si vacancies are generally unstable (e.g., Stocker and Smyth, 1978).

4.3. Defect evolution during dehydration of Kilauea Iki olivine

Fig. 14 illustrates the potential initial defects and mode of H^+ reorganization in Kiki and how different this reorganization is from San Carlos. After 8 h of heating at 800 °C, Kiki shows a clear decrease in the [Fe^{3+}-H] peak intensity and mirrored increase in the [Si-4H] intensity, while the [Ti-2H] peaks and total H^+ were essentially immobile (Fig. 9), in striking contrast to the clear loss in [Ti-2H] from San Carlos olivine SC1-2 under the same experimental conditions (Fig. 7). These results suggest that Kiki underwent an initial redistribution of H^+ prior to H^+ loss. One possible explanation (Fig. 14A and B) may be described broadly as

$$\left[\mathrm{Si}-4\mathrm{Fe}^{3+}\right]+4\left[\mathrm{Fe}^{3+}-\mathrm{H}\right]\rightarrow[\mathrm{Si}-4\mathrm{H}]+4\left[\mathrm{M}-2\mathrm{Fe}^{3+}\right] \quad (4a)$$

and may be described in Kröger-Vink notation as

$$\left\{V''''_{Si}-4Fe^{\bullet}_{M}\right\}+4\left\{Fe^{\bullet}_{M}-V''_{M}-OH^{\bullet}_{O}\right\}\rightarrow\left\{V''''_{Si}-4OH^{\bullet}_{O}\right\}+4\left\{2Fe^{\bullet}_{M}-V''_{M}\right\} \quad (4b)$$

and in terms of olivine formula units as

$$\mathrm{Fe_4SiO_8}+4\mathrm{FeHSiO_4}+3\mathrm{Mg_2SiO_4}\rightarrow\mathrm{Mg_2H_4O_4}+4\mathrm{MgFe_2Si_2O_8} \quad (4c)$$

Eq. (4) implies the initial presence of anhydrous Si vacancies, which, as mentioned in the above discussion on San Carlos olivine, is generally unfavorable. Our observation of H^+-related FTIR peaks shifting rapidly to peaks associated with hydrous Si vacancies suggests that such defects can and do occur. The magmatic host with which the Kilauea Iki olivine equilibrated was significantly oxidized (FMQ + 0.4, Helz et al., 2017), and, unlike the San Carlos xenolith, the Kiki volcanic phenocryst was rapidly quenched in minutes in a fire fountain (Newcombe et al., 2017b). These conditions would have led to an abundance of Fe^{3+} in the initial Kiki, which may have both stabilized anhydrous Si vacancies and impeded loss from Ti-defects (the reverse of Eq. (2)) in the lower temperature experiments (800 °C). Alternatives to Eq. (4) might also be possible, e.g., with initial Fe^{3+} on Si sites charge-balanced with trivalent cations on metal sites, but this example would require extremely rapid movement of the Fe, not just the hydrogen.

After the H^+ redistributed between sites and the temperature was increased to 1000 °C, the [Ti-2H] exhibited fast, anisotropic loss profiles from Kiki (Fig. 10). The reason

for this jump in the [Ti-2H] mobility rate, from essentially immobile (at or near the PV rate) to noticeable H^+ loss at the redox rate, is not entirely clear but may be related to changes in the defect structure of Kiki. At higher temperatures, the sphere of availability of Fe^{2+} might have been greater, enabling H^+ to exit [Ti-2H] once again at the redox rate.

4.4. Achieving steady-state rates between the redox rate and PV during dehydration

We observe diffusivities significantly higher than those expected for vacancy-facilitated diffusion measured in synthetic forsterite (Fig. 12), which suggests that at least one mechanism is occurring that involves only the movement of H^+ and electrons, the classic redox mechanism: $2H^+ + 2Fe^{2+} \rightarrow H_2 + 2Fe^{3+}$ (Kohlstedt and Mackwell, 1998). The relationship between this rapid process and purely vacancy-facilitated diffusion is traditionally understood in terms of an abrupt transition, a sort of light switch that is set to either on or off, at rates equal to either redox or PV. This clear transition has been observed for hydration (Kohlstedt and Mackwell, 1998; Demouchy and Mackwell, 2006; this study Fig. 5), but our dehydration data are not fully consistent with this model in terms of either edge concentrations or the rate of change in the diffusivities. Thoraval and Demouchy (2014) model profiles expected for such a transition (their Fig. 6). Their models predict a fairly close equivalent to the metastable equilibrium concentration of hydration, in which very early stage dehydration profiles are not particularly well developed near the edge, reach a stage in which the profile is relatively flat with very steep drops on the edges, and then proceeds to drop at the PV rate. The Kilauea Iki total H^+ profiles change very little during initial heating at 800 °C, when Thoraval and Demouchy suggest that rapid redox rate diffusion should be occurring, and then at 1000 °C we observe the rapid development of profiles that appear to go to zero and show a fairly consistent diffusivity over time. The SC1-2 data had an initial hydrated concentration at metastable equilibrium rather than full solubility and might be expected to only proceed at the redox rate until all of the H^+ had returned to its untreated level. Instead, the total H^+ diffusivity in SC1-2 appears to slow down over time. The behavior of H^+ thus appears to be fundamentally different during dehydration than what might be expected from hydration experiments.

One possible explanation is that the initial rapid hydration of San Carlos at the redox rate is limited by the initial abundance of Fe^{3+} in olivine, which is below detection limits for Mössbauer spectroscopy (Dyar et al., 1989). Once the Fe^{3+} is consumed, hydration at the redox rate (Eq. (2)) must cease. This is not the case for dehydration, where wt% levels of Fe^{2+} are always present to drive Eq. (2) backwards. Thus, while we see rate changes during dehydration that are likely due to the reorganization of H^+ and the effective proximity of Fe^{2+}, there is no shut-down as in hydration.

We can also understand the difference in behavior for SC1-2 (decreasing diffusivities with time from fast to relatively slow) and Kiki at 1000 °C (constant relatively slow diffusivities) as a difference in initial Fe^{3+} concentrations,

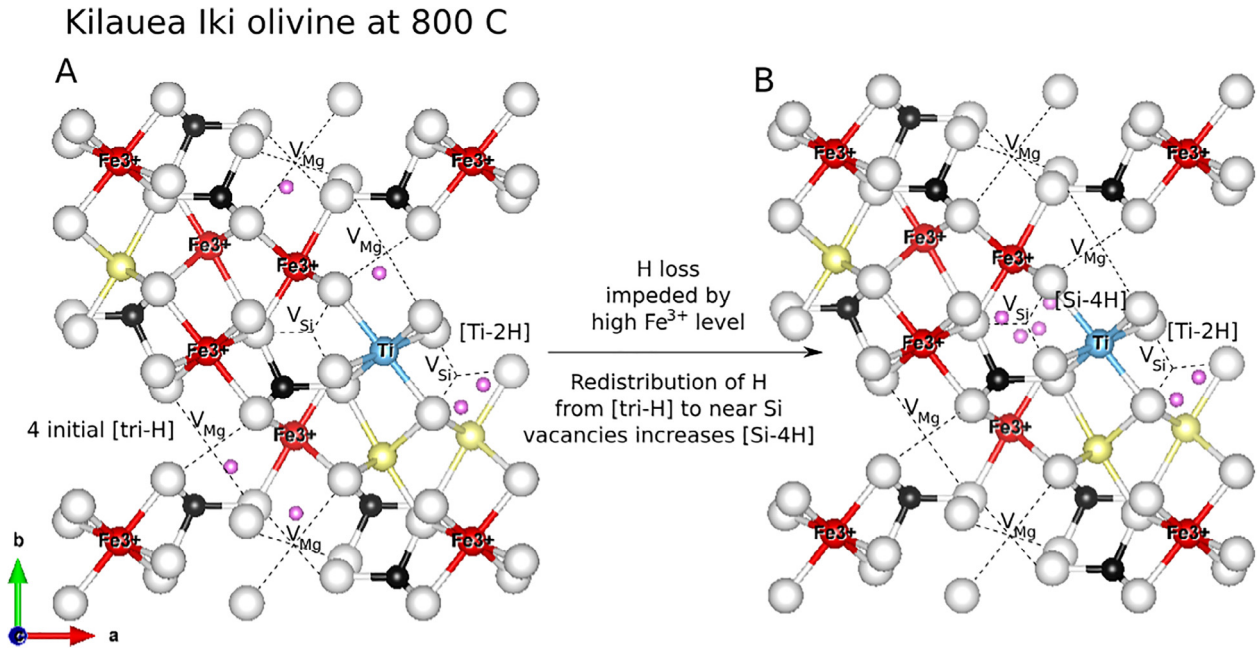

Fig. 14. Crystal models illustrating defects in the Kilauea Iki olivine before (A) and after (B) heating at 800 °C for 7 h in a 1-atm gas-mixing furnace. Defect labels are explained in Table 1. Ball colors corresponds to the following: yellow is Mg; grey is O; black is Si; blue is Ti, pink is H, and red is Fe^{3+}. Note that this figure is intended only to provide a general illustration of the defects and reaction described in Eq. (4), and Fe^{3+} is likely to be much less concentrated in a real crystal. Crystal images were created using VESTA (Momma and Izumi, 2011). (For interpretation of the references to colour in this figure legend, the reader is referred to the web version of this article.)

with SC1-2 starting with little active Fe^{3+} (having just reduced the sample during hydration) and thus experiencing more initial H^+ loss at the redox rate. In contrast, redox-rate loss of H^+ may have been impeded in the significantly oxidized Kilauea Iki olivine (FMQ + 0.4, Helz et al., 2017). Because of this decrease in the total H^+ diffusivity, the transition from the redox rate to the PV rate during dehydration is less like a light switch and more like a dimmer switch, with a top setting of the redox rate and bottom setting of the PV rate.

However, this dimmer switch analogy is not perfect because, as described in the previous two sections, variations in H^+ diffusivities are also affected by changes in the ferric/ferrous ratio and a competition between dehydration and rehydration associated with H^+ redistribution among defect sites. The fact that we are able to come up with a common set of Arrhenius laws also suggests that at some point a steady state is reached intermediate between the redox rate and PV. We relate this steady-state rate to the coupling of Eqs. (2) and (4), in which the overall rate-determining step is the movement of H^+ from one site to another.

One alternative possible explanation for the apparent convergence of total H^+ rates is that the H^+ loss rate may be set by the rate at which the ferric/ferrous iron ratio equilibrates with the fO_2 external to the sample. Such re-equilibration is known to occur (Gaetani et al., 2012) and could reduce the Fe and allow redox-rate diffusion to continue where it might otherwise have stopped on account of a local over-abundance of Fe^{3+}. Once a given olivine's ability to accept Fe^{3+} has been saturated, the redox-rate in that olivine will then be limited by the rate at which Fe^{3+} can be re-introduced. However, fO_2 equilibration in the center of the crystal may be slow (Faul et al., 2018), and H^+ diffusivities have been consistently observed to be independent of fO_2 (see Mackwell and Kohlstedt, 1990, Kilauea Iki in this study, and the differences in fO_2 among the melt inclusion studies shown in Fig. 12) which suggest that the equilibration with the external fO_2 during these experiments is too slow to have a significant impact on the measured diffusivities. However, the Fe^{3+}/Fe^{2+} ratio and total Fe content does appear to be important for determining H^+ behavior (e.g., the difference between H^+ mobility in the Kilauea Iki and San Carlos olivines at 800 °C). Thus, the fO_2 at which a sample is initially equilibrated likely is important for determining the apparent H^+ diffusivity, but the fO_2 at which the experiment is conducted may not have time to equilibrate with the sample.

4.5. Comparison with previous work for total H^+

Our final total H^+ diffusivities for all three crystals (Fig. 12) are consistent with the large majority of previous observations of H^+ movement out of Fe-bearing olivines in nature. Thoraval and Demouchy (2014) extensively discuss 1- and 3-dimensional modeling of FTIR profiles of natural dehydrated olivine, with specific application to H^+ profiles in Pali-aike olivine measured by Demouchy et al., 2006 and including discussion of H^+ profiles measured by Peslier and Luhr (2006) and Denis et al. (2013). They conclude "The concentration profiles measured for Pali-aike samples are characteristic of dehydration. However, they are neither consistent with redox process, which is too fast, nor with PV process, since a fast [001] axis is not observed." Profiles reported in Peslier et al. (2008) and Peslier et al. (2015) could also be reasonably interpreted as having a fast direction ∥ *a* rather than ∥ *c*. Our experimental results are fully consist with the many observations in natural samples of dehydration intermediate between redox and PV rates and with a fast direction ∥ *a*.

Our proposed Arrhenius laws are also consistent with the observation of H^+ distribution in and around melt inclusions by Le Voyer et al. (2014) and Lloyd et al. (2013). Le Voyer et al. (2014) used the NanoSIMS to map total H^+ around an olivine-hosted melt inclusion and found strongly anisotropic zonation with an inferred fast direction of H-loss parallel to *a*. They interpreted this observed anisotropy as dehydration at the redox rate, but the results presented here demonstrate that dehydration can occur with a fast direction ∥ *a* and diffusivities lower than the redox rate. Lloyd et al. (2013) document water loss from olivine-hosted melt inclusions as a function of the size of the pyroclast. The decompression rates determined from melt embayments from the same samples (Lloyd et al., 2014) are more consistent with H^+ loss from the melt inclusions through the olivine at close to the redox rate than to the PV rate and are consistent with our proposed Arrhenius laws.

Hauri (2002), Portnyagin et al. (2008), Chen et al. (2011), Gaetani et al. (2012), and Mironov et al. (2015) use changes in the water concentration in the melt inclusions in unoriented olivines to estimate H^+ diffusivities in natural olivine. As discussed in some detail by Chen et al. (2011), diffusive anisotropy is very difficult to account for in these experiments, and the resulting estimates are likely to fall somewhere between the fast and slow direction diffusivities. Indeed, six of the seven diffusivity estimates produced from these melt inclusions studies fall between our estimated fast direction diffusivities ∥ *a* and our slower direction diffusivities (Fig. 12). Thus, the H^+ diffusivity estimates from Portnyagin et al. (2008), Chen et al. (2011), Gaetani et al. (2012), and Mironov et al. (2015) are all fully consistent with the results presented here. This agreement is remarkable given the wide variety of experimental conditions represented by these efforts, including both hydration and dehydration and oxygen fugacities ranging from QFM-7 (Chen et al., 2011) to QFM + 3.3 (Portnyagin et al., 2008). Such similarity in inferred diffusivity over 10 log units of fO_2 suggests either that fO_2 does not affect H^+ diffusivity (which we find unlikely, given the close coupling to Fe redox), or, as mentioned above, that externally imposed fO_2 in many experimental assemblies does not equilibrate with the sample interior as rapidly as H^+ reacts and moves through the lattice. The latter view is supported by recent work (Jollands et al., 2018; Faul et al., 2018) that suggests fO_2 equilibration may proceed at the slower rate of metal vacancy diffusion and thus will be incomplete in many laboratory experiments.

The only exception to the broad agreement of the above studies is a single, very fast estimate by Hauri (2002) for the

dehydration of a melt-inclusion-bearing olivine from Loihi. This very rapid movement is difficult to understand with any certainty in the absence of either oriented profiles or FTIR spectra, and in the absence of measurements of crystal or melt inclusion sizes. The diffusivities calculated in Hauri (2002) also did not take into account the very low partitioning of water in olivine, which plays an important role in impeding melt inclusion water loss through the olivine (e.g., Chen et al., 2011). We conclude that the diffusivity determined in Hauri (2002) is highly uncertain and could reflect rates similar to those inferred for the other studies of melt inclusion re-equilibration shown in Fig. 12.

Finally, we also note a coherence between our proposed Arrhenius laws and those for H-D self-diffusion determined by Du Frane and Tyburczy (2012) and Novella et al. (2017). In these experiments, San Carlos was first dry-annealed, then wet annealed at the redox rate, then wet annealed again within a bath of heavy H_2O. The rate at which D entered the olivine was interpreted as the H-D exchange rate and proceeded along Arrhenius laws remarkably similar to ours for dehydration (Fig. 12). Given that the mechanism of H loss and D gain is largely one of exchange between defect sites, the results of these exchange experiments may be similar to the rate of reorganization that we have interpreted to be the control on total H loss from olivine.

While more work remains to be done to better understand and predict the variations in the rate of H loss from olivine, the frequent observation of rapid H^+ loss and anisotropy from natural samples suggests that at least some of the H^+ in a typical olivine dehydrating upon ascent is exiting at the redox rate, resulting in H^+ diffusion with a fast direction ‖ *a*. In almost all cases, the total diffusivity of H^+ in olivine occurs at rates between the redox and the PV rates.

4.6. Comparison with previous work on peak-specific behavior

Changes in FTIR spectra show that H^+ loss or gain occurs at different rates for different incorporation mechanisms (Figs. 7–10; Padrón-Navarta et al., 2014; Hilchie et al., 2014; Tollan et al., 2015; Peslier et al., 2015; Jollands et al., 2016). Most of the peak-specific H^+ diffusivities observed in this study are orders of magnitude higher than any of the diffusivities observed in synthetic forsterite (Fig. 12). Peak-specific diffusivities may also change over time (Fig. 8), most likely due to a redistribution of H^+ among different defects and discussed further below. Thus, single values for peak-specific diffusivities measured in synthetic forsterite (Padrón-Navarta et al., 2014; Jollands et al., 2016), may not apply to natural Fe-bearing olivines where H^+ mobility at or near the redox rate is taking place and an increased number of defects and higher vacancy concentrations may speed up vacancy-facilitated diffusion.

Padrón-Navarta et al. (2014), Hilchie et al. (2014), and Peslier et al. (2015) all observe faster movement of Mg-vacancy-related defects [Mg-2H] and/or [Fe^{3+}-H] relative to Si-vacancy-related defects [Ti-2H] and [Si-4H] during dehydration. This observation is echoed in our hydration data for SC1-7 (Fig. 5) but we were unable to test this result during dehydration of our SC1-2 sample because these peaks were either not present ([Mg-2H]) or not systematically present ([Fe^{3+}-H]).

During the sequential dehydration of the Kilauea Iki olivine, we observe a clear fast direction ‖ *a* in the movement of the peaks related to [Si-4H] and [Ti-2H] but not for the peaks related to [Fe^{3+}-H], which produce noisy, isotropic profiles with diffusivities that are, while still faster than would be expected from vacancy-controlled diffusivities in forsterite, roughly an order of magnitude slower ‖ *a* than the [Ti-2H] and [Si-4H] peaks. This result is in contrast to the observations of faster [Fe^{3+}-H] movement by other authors. The difference in anisotropy also suggests that the dominant mechanism by which H^+ in our Iki sample leaves [Fe^{3+}-H] is different from how it leaves [Ti-2H] and [Si-4H]. Perhaps, for instance, H^+ leaves [Ti-2H] and [Si-4H] primarily at the redox rate but leaves [Fe^{3+}-H] primarily during some redistribution process, for instance by moving from a Mg vacancy to a Si vacancy.

The SC1-2 partial hydration to metastable equilibrium resulted in minuscule amounts of [Mg-2H] and [Fe^{3+}-H] (Figs. 4 and 5) too small to give meaningful diffusivities during dehydration. The absence of these peaks from SC1-2 and large increase in [Ti-2H] suggest that in San Carlos olivine, the vast majority of H^+ diffusion at the redox rate is affecting the [Ti-2H] specifically. This observation is in stark contrast to >4 orders of magnitude lower rate of [Ti-2H] dehydration measured by Padrón-Navarta et al. (2014) in Fe-free synthetic forsterite. This result underscores the lack of inherent peak-specific rates and the importance of Fe in allowing H^+ to exit quickly from any site via reorganization (similar to results for clinopyroxene, Stalder et al., 2007; Ferriss et al., 2016). Padrón-Navarta et al. (2014) found a similar importance for reorganization, where [Si-4H] initially dehydrated as rapidly as [Ti-2H], but without Fe, all diffusivities were limited to the next fastest rate, that of metal vacancies. The fact that H^+ is able to enter San Carlos olivine so quickly in the first hours of hydration at the redox rate suggests that at least some octahedral Ti is initially present in San Carlos olivine. If all of the Ti were on the tetrahedral site initially, then some of that Ti would need to change its position in the crystal to create the [Ti-2H] defect, a process that we consider unlikely to occur under the hour timescales at which diffusion is observed (see discussion in Section 4.2). Octahedral Ti may be incorporated into the San Carlos olivine at depth during slow hydration reactions (e.g., following the reverse of the reaction described by Padrón-Navarta et al., 2014 Eq. (3b)) followed by rapid dehydration and quenching in a lava flow. Thus, any rapid influx of H^+ at the redox rate into an olivine may be limited not only by the initial quantity of Fe^{3+} (Kohlstedt and Mackwell, 1998) but the initial amount of octahedral Ti.

The convergence of peak-specific rates in San Carlos olivine (Fig. 8) suggests that in some applications peak-specific behavior may be safely ignored. An important exception may be the high-wavenumber [Si-4H] peaks such as 3600 cm^{-1} peak in the San Carlos olivine described here and the 3613 cm^{-1} peak in forsterite

described by Padrón-Navarta et al. (2014). These peaks never came close to a rim concentration of zero in either of these experiments, and they were particularly slow moving during early stages of dehydration. However, the 3600 cm^{-1} peak first rises (at 800 °C) and then drops (at 1000 °C) significantly in the Kilauea Iki olivine, indicating that it can sometimes increase or decrease relatively rapidly. Additional work to understand peak-specific behavior is warranted, and any workers concerned with H^+ diffusion in or out of olivine or olivine-hosted melt inclusions should routinely obtain polarized FTIR profiles to help determine the importance of differences in individual peak behavior for a given olivine.

5. CONCLUSIONS

We conducted a series of hydration and dehydration experiments to gain insight into the behavior of H^+ in natural olivine. The results show strikingly different behavior from previous studies, which focused on either hydration only or on Fe-free olivine. We also discovered a rich range of behavior even for just the two olivines used in our study. H^+ can speed up or slow down as it exits olivine and move at rates that depend on the evolving defect structure. Nonetheless, our results point to a common working rate of H loss for olivines with Fo85-90 that have been studied experimentally. While there is still much that we do not understand, and more work is welcomed on the experimental dehydration of a range of olivine compositions and on the analytical challenge of measuring Fe^{3+} in olivine, we can however draw three conclusions with some certainty.

First, there is no inherent diffusivity for specific H defects in olivine. For example, the Ti-clinohumite defect in olivine, [Ti-2H], which may influence the rheology of the upper mantle (Walker et al., 2007; Faul et al., 2016), loses H^+ at a rate that can vary by more than 4 orders of magnitude, depending on the Fe concentration and local Fe^{2+}/Fe^{3+} distribution. We found that [Ti-2H] can dehydrate or hydrate at or near the fastest redox rate in olivine. H^+ movement into and out of this defect at these very fast rates suggests that the Ti is present initially in an octahedral rather than tetrahedral site because the movement of H^+ is too rapid to allow for a reaction to occur in which Ti, or any other large ion, can move between sites. Thus, rapid hydration of olivine depends at least partially on the initial concentration of octahedral Ti. In the case of San Carlos olivine, which is commonly studied, its cooling history may already have pre-conditioned it for rapid hydration, due to rapid cooling and dehydration in lava that froze in octahedral Ti already associated with Fe^{3+}.

Second, the rates at which both total H^+ and individual defects sites move can change over time and depend on the defect population of the crystal. Thus, the use of constant peak-specific diffusivities measured in synthetic forsterite, e.g., as measured by Padrón-Navarta et al. (2014) and applied in Tollan et al. (2015), is inappropriate for natural, Fe-bearing samples. Further, the changes in total H^+ diffusivities observed here for dehydration are different from those observed here and elsewhere for hydration. Moreover, the binary change of rates from redox to proton-vacancy suggested by Thoraval and Demouchy (2014) based on observations of hydration are not observed in our dehydration experiments. Instead, the buildup of Fe^{3+} and redistribution of H^+ defects effectively slow down dehydration from redox rates, somewhat similar to the shifts in H_2O-OH internal equilibria with concentration during rhyolite dehydration (Zhang et al., 1991).

Third, there appears to be a common set of Arrhenius laws that can be used to explain most experimental and natural data for H^+ loss from Fo 85–90 olivine: $D_a = 10^{-5.4}\exp(-130/RT)$; $D_b = 10^{-6.9}\exp(-130/RT)$; and $D_c = 10^{-6.6}\exp(-130/RT)$, where the units of the diffusivities are in m^2/s, and the activation energy, 130, is in kJ/mol. These Arrhenius laws are intermediate between the classic redox and PV models of diffusivity observed during hydration and are in good agreement with many observations of a fast direction $\| a$ in natural olivine. While variations in different H^+ incorporation mechanisms and other defects may produce potentially large variations in the total H^+ diffusivities for different olivines, the working total H^+ Arrhenius laws determined here are expected to apply to most natural olivines.

Our results on H^+ diffusion in olivine find close parallels in the study of pyroxenes. Woods et al. (2000) point to an important threshold Fe content that leads to rapid total H diffusion in clinopyroxene. Stalder et al. (2007) demonstrate the importance of rapid reaction between defects, reorganization and redox reactions, documented by Mössbauer spectroscopy, during hydration and dehydration of Fe-bearing enstatite. Our own work (Ferriss et al., 2016) shows how peak-specific diffusivities become less important, uniformly faster, and approach the redox rate with greater Fe content in clinopyroxene.

The uniformly rapid rates of H^+ loss from olivine during ascent and cooling have two major implications. First, olivines in mantle xenoliths are likely to reach a steady-state on time scales of minutes to hours rather than days, as suggested by previous work on dehydration of synthetic forsterite (Padrón-Navarta et al., 2014). Thus, it is possible that the H^+ in olivine from many xenoliths has re-equilibrated with the host magma during the hours to days of transport to the surface (Ferriss et al., 2016). Systematic study of mantle xenoliths and host magmas are necessary to assess this possibility. Second, H^+ profiles in olivine, both in phenocrysts and in xenoliths, are of great practical use for ascent chronometry, and with the H^+ diffusivities known, measurements of H^+ profiles in olivine can now be used to access hours-to-minute timescales of magma ascent prior to explosive eruptions (Newcombe et al., 2017a).

ACKNOWLEDGMENTS

This manuscript benefited from constructive, thorough reviews by Sylvie Demouchy, Michael Jollands, and F.J. Ryerson, as well as the editorial work of Andrew Campbell. This work was supported primarily by National Science Foundation (NSF) Grant #1449699 to Elizabeth Ferriss as well as Grant #1551868 to Megan Newcombe, Grant #1145177 to Terry Plank for the Kilauea samples and analyses, and Grant #EAR-1731784 to Plank for study of water in mantle xenoliths. David Kohlstedt provided the San

Carlos sample and David Ferguson provided the Kilauea Iki samples, which Bruce Houghton collected. Daniel Rasmussen performed the electron microprobe analyses. Henry Towbin and Anna Barth performed the EBSD analyses to confirm sample orientations. Weathers Maura assisted in the use of the Laue Camera at Cornell Center for Materials Research Shared Facilities which are supported through the NSF MRSEC program (DMR-1719875). Erik Hauri performed the NanoSIMS analyses as part of a Cooperative Institute for Dynamic Earth Research (CIDER) working group on the electrical conductivity of hydrous olivine.

APPENDIX A. SUPPLEMENTARY MATERIAL

Supplementary data to this article can be found online at https://doi.org/10.1016/j.gca.2018.08.050.

REFERENCES

Bai Q. and Kohlstedt D. L. (1993) Effects of chemical environment on the solubility and incorporation mechanism for hydrogen in olivine. *Phys. Chem. Miner.* **19**, 460–471.

Bell D. R. and Rossman G. R. (1992) Water in Earth's mantle: the role of nominally anhydrous minerals. *Science* **255**, 1391–1397.

Bell D. R., Rossman G. R., Maldener J., Endisch D. and Rauch F. (2003) Hydroxide in olivine: a quantitative determination of the absolute amount and calibration of the IR spectrum. *J. Geophys. Res Solid Earth*, 108.

Beran A. and Putnis A. (1983) A model of the OH position in olivine, derived from infrared spectroscopy investigations. *Phys. Chem. Miner.* **9**, 57–60.

Beran A. and Zemman J. (1969) Üder OH-gruppen in Olivin. *Österreich Akademie des Wissenschaften* **3**, 73–74.

Berry A. J., Hermann J., O'Neill H. S. C. and Foran G. J. (2005) Fingerprinting the water site in mantle olivine. *Geology* **33**, 869–872.

Berry A. J., O'Neill H. S. C., Hermann J. and Scott D. R. (2007a) The infrared signature of water associated with trivalent cations in olivine. *Earth Planet. Sci. Lett.* **261**, 134–142.

Berry A. J., Walker A. M., Hermann J., O'Neill H. S., Foran G. J. and Gale J. D. (2007b) Titanium substitution mechanisms in forsterite. *Chem. Geol.* **242**, 176–186.

Blanchard M., Ingrin J., Balan E., Kovács I. and Withers A. C. (2017) Effect of iron and trivalent cations on OH defects in olivine. *Am. Mineral.* **102**, 302–311.

Carslaw H. S. and Jaeger J. C. (1959) Conduction of Heat in Solids. Clarendon, Oxford, U.K..

Chen Y., Provost A., Schiano P. and Cluzel N. (2011) The rate of water loss from olivine-hosted melt inclusions. *Contrib. Miner. Petrol.* **162**, 625–636.

Cherniak D. J. and Liang Y. (2014) Titanium diffusion in olivine. *Geochim. Cosmochim. Ac.* **147**, 43–57.

Demouchy S. and Mackwell S. (2003) Water diffusion in synthetic iron-free forsterite. *Phys. Chem. Miner.* **30**, 486–494.

Demouchy S. and Mackwell S. (2006) Mechanisms of hydrogen incorporation and diffusion in iron-bearing olivine. *Phys. Chem. Miner.* **33**, 347–355.

Demouchy S. and Bolfan-Casanova N. (2016) Distribution and transport of hydrogen in the lithospheric mantle: a review. *Lithos* **240**, 402–425.

Demouchy S., Jacobsen S. D., Gaillard F. and Stern C. R. (2006) Rapid magma ascent recorded by water diffusion profiles in mantle olivine. *Geology* **34**, 429–432.

Demouchy S., Thoraval C., Bolfan-Casanova N. and Manthilake G. (2016) Diffusivity of hydrogen in iron-bearing olivine at 3 GPa. *Phys. Earth Planet. Interiors* **260**, 1–13.

Denis C. M. M., Demouchy S. and Shaw C. S. J. (2013) Evidence of dehydration in peridotites from Eifel Volcanic Field and estimates of the rate of magma ascent. *J. Volcanol. Geoth. Res.* **258**, 85–99.

Du Frane W. L. and Tyburczy J. A. (2012) Deuterium-hydrogen exchange in olivine: implications for point defects and electrical conductivity. *Geochem. Geophys. Geosyst.* **13**, 1–12.

Dyar M. D., McGuire A. V. and Ziegler R. D. (1989) Redox equilibria and crystal-chemistry of coexisting minerals from spinel lherzolite mantle xenoliths. *Am. Mineral.* **74**, 969–980.

Faul U. H., Cline, II, C. J., David E. C., Berry A. J. and Jackson I. (2016) Titanium-hydroxyl defect-controlled rheology of the Earth's upper mantle. *Earth Planet. Sci. Lett.* **452**, 227–237.

Faul U. H., Cline, II, C. J., Berry A., Jackson I. and Garapíc G. (June 2018) Constraints on oxygen fugacity within metal capsules. *Phys. Chem. Miner.* **45**(June), 497–509.

Ferguson D. J., Gonnermann H. M., Ruprecht P., Plank T., Hauri E. H., Houghton B. F. and Swanson D. A. (2016) Magma decompression rates during explosive eruptions of Kīlauea volcano, Hawaii, recorded by melt embayments. *Bull. Volcanol.* **78**, 71.

Ferriss E. (2018) Pynams: A Python package for interpreting FTIR spectra of nominally anhydrous minerals (NAMs) (Version v2.1). Zenodo. http://doi.org/10.5281/zenodo.594184.

Ferriss E., Plank T., Walker D. and Nettles M. (2015) The whole-block approach to measuring hydrogen diffusivity in nominally anhydrous minerals. *Am. Mineral.* **100**, 837–851.

Ferriss E., Plank T. and Walker D. (2016) Site-specific hydrogen diffusion rates during clinopyroxene dehydration. *Contrib. Miner. Petrol.* **171**, 1–24.

Ferriss E., Newcombe M. (2018) Data and code for H diffusion in olivine (Version v1.1). Zenodo. http://doi.org/10.5281/zenodo.1318324.

Gaetani G. A., O'Leary J. A., Shimizu N., Bucholz C. E. and Newville M. (2012) Rapid reequilibration of H_2O and oxygen fugacity in olivine-hosted melt inclusions. *Geology* **40**, 915–918.

Gaetani G. A., O'Leary J. A., Koga K. T., Hauri E. H., Rose-Koga E. F. and Monteleone B. D. (2014) Hydration of mantle olivine under variable water and oxygen fugacity conditions. *Contrib. Miner. Petrol.* **167**, 965.

Hauri E. (2002) SIMS analysis of volatiles in silicate glasses, 2: isotopes and abundances in Hawaiian melt inclusions. *Chem. Geol.* **183**, 115–141.

Helz R. T., Cottrell E., Brounce M. N. and Kelley K. A. (2017) Olivine-melt relationships and syneruptive redox variations in the 1959 eruption of Kīlauea Volcano as revealed by XANES. *J. Volcanol. Geoth. Res.* **333–334**, 1–14.

Herd, C. D. K. (2008) Basalts as probes of planetary interior redox state. Book section in Oxygen in the solar system, Reviews in Mineralogy and Geochemistry. Mineralogical Society of America.

Hilchie L., Fedortchouk Y., Matveev S. and Kopylova M. G. (2014) The origin of high hydrogen content in kimberlitic olivine: evidence from hydroxyl zonation in olivine from kimberlites and mantle xenoliths. *Lithos* **202–203**, 429–441.

Houlier B. et al. (1990) Silicon diffusion in San Carlos olivine. *Phys. Earth Planet. Interiors* **62**(3–4), 329–340.

Ingrin J., Liu J., Depecker C., Kohn S. C., Balan E. and Grant K. J. (2013) Low-temperature evolution of OH bands in synthetic forsterite, implication for the nature of H defects at high pressure. *Phys. Chem. Miner.* **40**, 499–510.

Jollands M. C., Padrón-Navarta J. A., Hermann J. and O'Neill H. S. C. (2016) Hydrogen diffusion in Ti-doped forsterite and the preservation of metastable point defects. *Am. Mineral.* **101**, 1560–1570.

Jollands M. C., O'Neill H., Van Orman J., Berry A. J., Hermann J., Newville M. and Lanzirotti A. (2018) Substitution and diffusion of Cr^{2+} and Cr^{3+} in synthetic forsterite and natural olivine at 1200–1500 °C and 1 bar. *Geochim. Cosmochim. Acta* **220**, 407–428.

Kelley K. A., Plank T., Ludden J. and Staudigel H. (2003) Composition of altered oceanic crust at ODP Sites 801 and 1149. *Geochem. Geophys. Geosys.* **4**(6) (Data Brief).

Kohlstedt D. L. and Mackwell S. J. (1998) Diffusion of hydrogen and intrinsic point defects in olivine. *Z. Phys. Chem.* **207**, 147–162.

Kröger F. A. and Vink H. J. (1956) Relation between the concentrations of imperfections in crystalline solids. In *Solid State Physics*, vol. 3, p. 307. Solid State Physics. Academy Press, New York.

Le Voyer M., Asimow P. D., Mosenfelder J. L., Guan Y., Wallace P. J., Schiano P., Stolper E. M. and Eiler J. M. (2014) Zonation of H_2O and F Concentrations around Melt Inclusions in Olivines. *J. Petrol.* **55**, 685–707.

Libowitzky E. and Beran A. (1995) OH defects in forsterite. *Phys. Chem. Miner.* **22**, 387–392.

Libowitzky E. and Rossman G. R. (1996) Principles of quantitative absorbance measurements in anisotropic crystals. *Phys. Chem. Miner.* **23**, 319–327.

Lloyd A. S., Plank T., Ruprecht P., Hauri E. H. and Rose W. (2013) Volatile loss from melt inclusions in pyroclasts of differing sizes. *Contrib. Miner. Petrol.* **165**, 129–153.

Lloyd A. S., Ruprecht P., Hauri E. H., Rose W., Gonnermann H. M. and Plank T. (2014) NanoSIMS results from olivine-hosted melt embayments: magma ascent rate during explosive basaltic eruptions. *J. Volcanol. Geotherm. Res.* **283**, 1–18.

Long G. and Winefordner J. (1983) Limit of detection. A closer look at the IUPAC definition. *Anal. Chem.* **55**(7), 712A–724A.

Mackwell S. J., Dimos D. and Kohlstedt D. L. (1988) Transient creep of olivine: Point-defect relaxation times. *Philos. Mag.* **57** (5), 779–789.

Mackwell S. J. and Kohlstedt D. L. (1990) Diffusion of hydrogen in olivine - implications for water in the mantle. *J. Geophys. Res. Solid Earth* **95**, 5079–5088.

Mironov N., Portnyagin M., Botcharnikov R., Gurenko A., Hoernle K. and Holtz F. (2015) Quantification of the CO_2 budget and H_2O–CO_2 systematics in subduction-zone magmas through the experimental hydration of melt inclusions in olivine at high H_2O pressure. *Earth Planet. Sci. Lett.* **425**, 1–11.

Momma K. and Izumi F. (2011) Vesta 3 for three-dimensional visualization of crystal, volumetric and morphology data. *J. Appl. Crystallogr.* **44**, 1272–1276.

Mosenfelder J. L., Deligne N. I., Asimow P. D. and Rossman G. R. (2006) Hydrogen incorporation in olivine from 2–12. *Am. Mineral.* **91**, 285–294.

Mosenfelder J. L., Le Voyer M., Rossman G. R., Guan Y. B., Bell D. R., Asimow P. D. and Eiler J. M. (2011) Analysis of hydrogen in olivine by SIMS: Evaluation of standards and protocol. *Am. Mineral.* **96**, 1725–1741.

Nakamura A. and Schmalzried H. (1984) On the Fe^{2+} –Mg^{2+}-Interdiffusion in olivine (II). *Berich. Bunsengesell.* **88**(2), 140–145.

Newcombe M. N., Asimow P. D., Ferriss E., Barth A., Lloyd A. S., Hauri E. H. and Plank T. (2017a) Water-in-olivine magma ascent chronometry: every crystal is a clock. *AGU Fall Meeting, New Orleans, LA, Abstract V32A-03*.

Newcombe M., Lloyd A., Ferguson D., Barth A., Hauri E. and Plank T. (2017b) Syneruptive cooling rates and decompression rates of magmas from volcanoes with contrasting eruptive styles. *IAVCEI Meeting, Portland, OR, Submission 907*.

Novella D., Jacobsen B., Weber P. K., Tyburczy J. A., Ryerson F. J. and Du Frane W. L. D. (2017) Hydrogen self-diffusion in single crystal olivine and electrical conductivity of the Earth's mantle. *Sci. Rep.* **7**, 5344.

O'Neill H. S. C. (1987) Quartz-Fayalite-Iron and Quartz-Fayalite-Magnetite equilibria and the free energy of formation of fayalite (Fe_2SiO_4) and magnetite (Fe_3O_4). *Am Mineral.* **72**, 67–75.

Padrón-Navarta J. A., Hermann J. and O'Neill H. S. C. (2014) Site-specific hydrogen diffusion rates in forsterite. *Earth Planet. Sci. Lett.* **392**, 100–112.

Peslier A. H. and Luhr J. F. (2006) Hydrogen loss from olivines in mantle xenoliths from Simcoe (USA) and Mexico: mafic alkalic magma ascent rates and water budget of the sub-continental lithosphere. *Earth Planet. Sci. Lett.* **242**, 302–319.

Peslier A. H., Woodland A. B. and Wolff J. A. (2008) Fast kimberlite ascent rates estimated from hydrogen diffusion profiles in xenolithic mantle olivines from southern Africa. *Geochim. Cosmochim. Acta* **72**, 2711–2722.

Peslier A. H., Bizimis M. and Matney M. (2015) Water disequilibrium in olivines from Hawaiian peridotites: recent metasomatism, H diffusion and magma ascent rates. *Geochim. Cosmochim. Acta* **154**, 98–117.

Portnyagin M., Almeev R., Matveev S. and Holtz F. (2008) Experimental evidence for rapid water exchange between melt inclusions in olivine and host magma. *Earth Planet. Sci. Lett.* **272**, 541–552.

Rae A. S., Edmonds M., Maclennan J., Morgan D., Houghton B., Hartley M. E. and Sides I. (2016) Time scales of magma transport and mixing at Kīlauea Volcano, Hawai'i. *Geology* **44** (6), 463–466.

Regenauer-Lieb K. (2006). In *Book Section in Water in Nominally Anhydrous Minerals, Reviews in Mineralogy and Geochemistry* (eds. H. Keppler and J. R. Smyth). Mineralogical Society of America.

Ruprecht P. and Plank T. (2013) Feeding andesitic eruptions with a high-speed connection from the mantle. *Nature* **500**, 68–72.

Shea T., Costa F., Krimer D. and Hammer J. E. (2015) Accuracy of timescales retrieved from diffusion modeling in olivine: a 3D perspective. *Am. Mineral.* **100**, 2026–2042.

Shuai K. and Yang X. (2017) Quantitative analysis of H-species in anisotropic minerals by polarized infrared spectroscopy along three orthogonal directions. *Contrib. Miner. Petrol.* **172**, 14.

Stalder R., Purwin H. and Skogby H. (2007) Influence of Fe on hydrogen diffusivity in orthopyroxene. *Eur. J. Mineral.* **19**, 899–903.

Stocker R. and Smyth D. (1978) Effect of enstatite activity and oxygen partial pressure on the point-defect chemistry of olivine. *Phy. Earth Planet. Interiors* **16**(2), 145–156.

Stovall W., Houghton B., Gonnermann H., Fagents S. and Swanson D. (2011) Eruption dynamics of Hawaiian-style fountains: the case study of episode 1 of the Kilauea Iki 1959 eruption. *Bull. Volcanol.* **73**, 511–529.

Thoraval C. and Demouchy S. (2014) Numerical models of ionic diffusion in one and three dimensions: application to dehydration of mantle olivine. *Phys. Chem. Miner.* **41**, 709–723.

Tollan P. M. E., O'Neill H. S. C., Hermann J., Benedictus A. and Arculus R. J. (2015) Frozen melt-rock reaction in a peridotite xenolith from sub-arc mantle recorded by diffusion of trace elements and water in olivine. *Earth Planet. Sci. Lett.* **422**, 169–181.

Tollan P. M. E., Smith R., O'Neill H. S. C. and Hermann J. (2017) The responses of the four main substitution mechanisms of H in olivine to H_2O activity at 1050 °C and 3. *Progr. Earth Planet. Sci.* **4**, 14.

Walker A. M., Hermann J., Berry A. J. and O'Neill H. S. C. (2007) Three water sites in upper mantle olivine and the role of

titanium in the water weakening mechanism. *J. Geophys. Res Solid Earth*, 112.

Witham F., Blundy J., Kohn S. C., Lesne P., Dixon J., Churakov S. V. and Botcharnikov R. (2012) SolEx: a model for mixed COHSCl-volatile solubilities and exsolved gas compositions in basalt. *Comput Geosci* **45**, 87–97.

Withers A. C. (2013) The Pitzer and Sterner Equation of State for Water [WWW Document]. URL <http://www.geo.umn.edu/people/researchers/withe012/fugacity.htm> (accessed 8.6.13), <https://www.esci.umn.edu/people/researchers/withe012/fugacity.htm> (accessed 7.20.2018).

Woods S. C., Mackwell S. and Dyar D. (2000) Hydrogen in diopside: diffusion profiles. *Am. Miner.* **85**, 480–487.

Withers A. C., Bureau H., Raepsaet C. and Hirschmann M. M. (2012) Calibration of infrared spectroscopy by elastic recoil detection analysis of H in synthetic olivine. *Chem. Geol.* **334**, 92–98.

Zhang Y., Stolper E. and Wasserburg G. (1991) Diffusion of water in rhyolitic glasses. *Geochim. Cosmochim. Acta* **55**, 441–456.

Zhao Y.-H., Ginsberg S. B. and Kohlstedt D. L. (2004) Solubility of hydrogen in olivine: dependence on temperature and iron content. *Contrib. Miner. Petrol.* **147**, 155–161.

Associate editor: Andrew J. Campbell